

THESIS FOR THE DEGREE OF LICENTIATE OF TECHNOLOGY

Thermoplasmonic Effects in Microfluidic Systems

What happens when you shoot a CW laser at a gold nano-structure in water and turn the power up.

Steven Jones



Department of Physics
CHALMERS UNIVERSITY OF TECHNOLOGY
Gothenburg, Sweden 2019

Thermoplasmonic Effects in Microfluidic Systems
Steven Jones

© Steven Jones, 2019

Division of Bionanophotonics
Department of Physics
Chalmers University of Technology
SE-412 96 Göteborg
Sweden
Telephone: +46 (0)31 – 772 10 00

Printed in Sweden by
Chalmers Reproservice
Chalmers Tekniska Högskola
Göteborg, Sweden, 2019

Thermoplasmonic Effects in Microfluidic Systems

Steven Jones

Department of Physics

Chalmers University of Technology

Abstract

The field of plasmonics has enabled a plethora of scientific achievements over the past few decades. Such advances have been the result of the increased light-matter interaction that occurs over nanoscale dimensions facilitated by the localized plasmonic resonances supported by noble metal nanoparticles. These plasmonic resonances enable increased coupling of light between the near-field (where interesting phenomena occur) and the far field (where the signal can be easily detected). In this way a plasmonic structure acts as a localized transducer in microfluidic environments that are beneficial in many biological studies. The field of plasmonics has been hindered by the enhanced optical absorption that occurs within the metallic nanoparticles due to their finite electrical conductivity at optical frequencies. Absorption can lead to significant temperature increases which has thus far been considered a detrimental side effect of these plasmonic resonances.

Thermal effects in plasmonic systems have recently become an area of intense study in their own right. Thermoplasmonics involves studying the influence that a plasmonically supported localized temperature increase has on the surrounding environment. These thermal effects are an interesting field of study both for their implications in traditional optical-plasmonic-sensing schemes, as well as due to new and exciting thermally based applications. In this thesis I explore two such cases. First, the detrimental impact of thermoplasmonic effects in plasmonic-optical-tweezers. And second, the formation of small thermoplasmonic nanobubbles that may be utilized for active microfluidic manipulation.

In plasmonic-optical-trapping the electric field enhancement supported by a plasmonic antenna amplifies the optical gradient force thereby enabling incredibly small particles to be “held” by the antenna. However, the same phenomenon that enhanced the optical forces also increases the localized heating. Here I will show how the localized heating essentially negates a portion of the optical force amplification by increasing the Brownian motion of the trapped particle. Even more impactful is the formation of a thermal barrier that prohibits diffusive transport of analytes to the antenna thereby significantly decreasing the interaction probability. This thermal barrier was found to extend several microns from the antenna – far beyond the range of optical interactions.

One potentially advantageous utilization of thermoplasmonics is in bubble formation. The presence of a thermally generated bubble can induce incredibly fast fluid currents in the surrounding environment. One such utilization is towards mixing multiple fluid streams in microfluidic environments. However, most studies to date have focused on thermoplasmonic microbubbles which tend to be quasi-stable, therefore prohibiting high throughput applications. Here I will demonstrate how isolated plasmonic structures can form thermoplasmonic nanobubbles which are quickly decaying and therefore advantageous as active manipulation elements. Such bubbles were able to be modulated at frequencies up to a few kilohertz in water, several orders of magnitude greater than previously demonstrated.

Keywords: plasmonics, thermoplasmonics, thermophoresis, plasmonic bubbles

List of Publications

LIST OF PUBLICATIONS INCLUDED IN THIS THESIS

This thesis is based on the work contained in the following papers. Contributions by the author are included below each work.

- i. **Photothermal heating of plasmonic nanoantennas: influence on trapped particle dynamics and colloid distribution**
Steven Jones, Daniel Andrén, Pawel Karpinski, & Mikael Käll
ACS Photonics, 5, 7, 2018
- Contributed to conceptual design, built the experimental setup, designed and simulated plasmonic structures, created experimental control software, performed all optical experiments and data analysis, and wrote the initial manuscript.

- ii. **Ultrafast Modulation of Thermoplasmonic Nano-Bubbles in Water**
Steven Jones, Daniel Andrén, Tomasz J. Antosiewicz, & Mikael Käll
In Manuscript
- Contributed to conceptual design, built the experimental setup, designed and simulated plasmonic structures, created experimental control software, performed all optical experiments and data analysis, and wrote the initial manuscript.

LIST OF PUBLICATIONS NOT INCLUDED IN THIS THESIS

- i. **Optically controlled stochastic jumps of individual gold nanorod rotary motors**
Lei Shao, Daniel Andrén, Steven Jones, Peter Johansson, & Mikael Käll
Physical Review B, 98, 8, 2018

- ii. **Counter-Propagating Optical Trapping of Resonant Nanoparticles Using a Uniaxial Crystal**
Pawel Karpinski, Steven Jones, Daniel Andrén, & Mikael Käll
Laser & Photonics Reviews, 12, 9, 2018

- iii. **Surface Interactions of Gold Nanoparticle Optically Trapped Against an Interface**
Daniel Andrén, Nils Odebo Länk, Hana Šípová-Jungová, Steven Jones, & Mikael Käll
The Journal of Physical Chemistry C, 123, 2019

- iv. **Artificial inorganic nanomotors driven by light**
Hana Šípová-Jungová, Daniel Andrén, Steven Jones, & Mikael Käll
Submitted

- v. **Low-loss Hybrid High-index Dielectric Particles on a Mirror for Extreme Light Confinement**
Aili Maimaiti, Partha Patra, Steven Jones, Tomasz Antosiewicz, & Ruggero Verre
Submitted

Acknowledgements

Nothing happens in a vacuum (even though physicists love to make that approximation). As such, the work contained here has benefitted both directly and indirectly from countless others, some of whom I endeavour to mention here. Apologies to any I have omitted – you have not been forgotten.

First and foremost, I would like to start by thinking my parents. Your endless support and love have benefitted me throughout my life. I cannot even begin to express my gratitude.

Daniel, you truly are the golden boy. Your work ethic, readiness to help others, and general approach to life is beyond impressive. It's a pleasure to work beside you. I could fill pages expressing my gratitude for your support both inside and outside of the office; however, for the sake of brevity I will simply say: thanks!

Nils, best of luck in your post-Ph.D.-life. I have always been amazed by your fundamental understanding of electromagnetism. I am certain you will succeed in all your future adventures. More often than not I am at least a little jealous of your life with the farm and dogs. Hope to see you around buddy.

Battulga, you are science personified. Your approach to research is something I hope to incorporate into my own behaviour as a scientist. It is always a pleasure to discuss with you. My admiration for you knows no bounds.

Ruggero, congratulations on the baby, but please do not forget about your friends here at BNP. We need your love and support also.

Tomasz, it is always a pleasure to grab a beer with you and talk science. I'm very glad we finally got the chance to more formally work together. Looking forward to your next visit!

Hana, I have a ton of respect for you and look forward to following your career, you will go far. Your academic approach to motherhood is incredibly fun to watch by the way, and quite informative as well!

Mikael Käll, last but certainly not least. Your guidance has benefited me beyond measure during my studies thus far. I am forever grateful for the support and opportunities you have provided for me. When I reflect on my development as a researcher since starting in your group I am astounded at my (perceived) progression – I believe much of that is attributable to you. It is an absolute pleasure working for you.

Thanks to everyone else in the BNP group. This is a great place to work and grow, due to both the constituent members and the leadership, in equal parts.

Steven Jones
2019.07.17

If you're going to kill two birds with one stone, you better not miss.

Contents

1	Introduction	1
2	Theory	5
	2.1 Light-Matter Interaction.....	5
	2.1.1 Electromagnetic Waves	6
	2.1.2 Permittivity and Refractive Index	6
	2.1.3 Interaction Between an EMW and a Small Dielectric Sphere ..	7
	2.1.4 Localized Surface Plasmon Resonances	9
	2.2 Thermoplasmonics.....	10
	2.2.1 Steady-state	12
	2.2.2 Temporal Dynamics	14
	2.3 Thermophoresis.....	16
	2.4 Thermoplasmonic Bubbles.....	21
3	Experimental Methods	27
	3.1 Optical Trapping	27
	3.1.1 Plasmonic Optical Trapping.....	30
	3.2 Plasmonic Anti-Stokes Thermometry	30
	3.3 Observing Thermophoresis via Fluorescence Microscopy	32
	3.4 Observing Plasmonic Nano-Bubbles via Optical Backscattering .	37
4	Summary of Appended Papers	41
	4.1 Paper I: Photothermal Heating of Plasmonic Nanoantennas: Influence on Trapped Particle Dynamics and Colloid Distribution	41
	4.2 Paper II: Ultrafast Modulation of Thermoplasmonic Nano-Bubbles in Water	43
5	Conclusion & Outlook.....	45
	References	47

Thermoplasmonic Effects in Microfluidic Systems

1 Introduction

This thesis is about thermoplasmonic effects in microfluidic environments. But before I can talk about thermo-plasmonics I need to briefly mention plasmonics, and before I can talk about that I need to talk about light. Light (i.e. electromagnetic waves) is something we are all familiar with – it is how we view the world around us. For scientists, light is an incredibly useful tool since by looking at how things interact with light we can learn about what the material is made of and how it behaves. When scientists want to look at how light interacts with *small* things, they often use a microscope. However, there is a limit to how *small* something can be to resolve it with light. Even for a perfect microscope (i.e. free from all aberrations and with perfect collection efficiency), objects with features much smaller than one optical wavelength can typically not be resolved – they are said to be “diffraction limited”. This fundamental limit in the ability to focus light to an infinitesimal point is the reason that we cannot directly view things like proteins or atoms with an optical microscope and are required to use an electron microscope instead.

However, while far-field optics cannot focus light to an arbitrarily small region, other techniques can be used to monitor light-matter interaction within diffraction limited volumes. One such technique utilizes noble metal nanostructures known as plasmonic antennas. The field of plasmonics describes how tiny metal nanoparticles can interact strongly with light. A plasmonic particle basically acts like the antenna on a car but at a much smaller scale. While radio antennas are typically about a meter long and interact with low frequency light, plasmonic antennas are around ten million times smaller and interact with high frequency light. When excited by this high frequency light, the electrons in the plasmonic particle will oscillate; resulting in electric field enhancement that is confined very near to the surface of the plasmonic particle. Because of this enhancement/confinement, scientists can use these plasmonic antennas to couple light from the far-field to diffraction limited regions and optically probe interactions that occur at the surface of these metallic nanoparticles.

Although these plasmonic antennas have been incredibly useful in allowing scientists to investigate processes at diffraction limited length scales, the associated heat generation has often been ignored. While metals are generally viewed as being perfect electrical conductors, this is no longer true at optical excitation frequencies. When illuminated by visible light, the high frequency current oscillations within noble metals suffers from significant Ohmic dampening which results in substantial heat generation. Because these metallic nanostructures are often thermally insulated, the generated heat can result in a large local temperature increase. This temperature increase has

Introduction

often been seen as a disadvantage of these plasmonic antennas and a great deal of effort has been made to try and mitigate this heating.

It is true that the effect of this heating can sometimes be a hindrance; however, in recent years there has been a movement to try and utilize this heat to do something useful instead. This is the field of thermoplasmonics: the study of heat generated by optically excited metal nanoparticles and the effects on the surrounding environment. Both the good and the bad.

Often the good and the bad arise for the same reasons. For instance, light is essentially trapped near the surface of a plasmonic antenna (this was the whole reason for plasmonic in the first place); however, when the antenna gets hot the heat dissipates into the surroundings. This can be bad if you are trying to *look* at something that does not like being hot. Conversely, there are many emerging applications where a localized heat source can be advantageous, and thermoplasmonics provides a unique opportunity to achieve extreme heat localization.

To summarize this thesis let's start with a story. Imagine a small gold sphere on top of a glass microscope slide immersed in water. If you shoot a laser beam at this gold sphere it will start to get hot. As the gold sphere gets hot so does its environment and after a short while you will have a hot metal sphere surrounded by water. Close to the metal sphere the water is hot and further away the water is cool – this is a temperature gradient. Now, if you want to *look* at particles swimming around the metal sphere this might be bad, since most particles don't like to be hot and will swim away before you can look at them. But, conversely, if you want to make these swimming particles go to a certain place then you can just use your gold sphere to make the water hot everywhere you *don't* want the particles to be.

If you turn up the laser power the gold sphere will get hotter. Eventually it will get so hot that the water around it will vaporize and cause the sudden emergence of a bubble. Now that you have a bubble surrounding your gold sphere the system has completely changed and new things begin to happen. First, because the bubble is mostly gas, it will trap the heat in the gold sphere making it get even hotter. In fact, it can get so hot that it can even destroy the gold sphere. However, it's also possible to allow the heat to escape in other ways to prevent this damage. If you do that, then this bubble can be very useful. Because one part of the bubble is slightly colder than another part, the water itself will be pulled towards the cold side. This creates a flow of water around the bubble. In this way your new bubble can act as a local pump that moves things around. If you turn off the laser, the temperature decreases and the bubble disappears along with the water currents. Essentially you have just made an optical switch for quickly moving water around in your microfluidic system.

Introduction

The study of thermoplasmonics contains a lot of these good/bad dichotomies. There are many effects that need to be studied so that they can be mitigated or accounted for. But there are often even more ways that these effects can be utilized for new and exciting opportunities. This thesis attempts to provide a fundamental overview of some such thermoplasmonic phenomena and presents some recent results that explores these thermal effects: both the good and the bad.

2 Theory

This chapter briefly outlines the theoretical foundation for thermoplasmonic systems and some of the associated effects in microfluidic environments. Section 2.1 introduces the concept of light-matter interaction. Beginning with the basic properties of electromagnetic waves including how they propagate in free space and how that propagation is affected when the wave propagates through a material. This concept is then extended to how a propagating wave interacts with small dielectric particles and how this interaction is greatly increased if the particle is instead a noble metal such as gold. This last subsection – the interaction of light with noble metal nanoparticles – is the field of plasmonics. When an electromagnetic wave excites plasmonic particles, the interaction is strongly enhanced and significant power is often absorbed.

In section 2.2 the thermal effects from this enhanced plasmonic absorption are explored. Because these small particles can absorb such significant amounts of heat they are able to produce large localized temperature increases in microfluidic systems. Both the steady state temperature profile and the temporal evolution of this temperature profile are examined.

In sections 2.3 and 2.4 two important thermally induced effects are introduced that form the fundamental components of this thesis. Thermophoresis (section 2.3) – the propensity of particle to move along a temperature gradient – is explained from a fundamental standpoint along with a brief overview of some recent works that utilize thermophoretic effects directly for various applications. Thermophoretic effects can often be detrimental in many optical manipulation and sensing schemes involving plasmonics but have hitherto been underexplored.

In section 2.4 we look at what happens if the temperature of a plasmonic particle is increased high enough such that bubble formation occurs. The presence of a bubble introduces exciting new physics into the system and has demonstrated a variety of appealing properties that may be useful in microfluidic environments. Section 2.4 details what is known about bubble formation and dissipation from recent studies on the topic of thermoplasmonically induced micro-bubbles as well as some notable applications of such bubbles.

2.1 Light-Matter Interaction

The study of light-matter interaction is a vast field that covers everything from the motion of a charged elementary particle in an oscillating electric field to exotic nonlinear effects such as second harmonic generation. Although a complete description of all such aspects of light-matter interaction is beyond the scope of this work, the following chapter attempts to provide a foundation for the concepts utilized in the rest of this thesis. This section begins with a

generic description of an electromagnetic wave (EMW) and how multiple waves can interact via superposition, here the concept of polarization is also introduced. In the following subsection optical properties of materials are introduced and how they affect light propagation. In 2.1.4 the interaction between small metal particles and light is explored – a field known as plasmonics.

2.1.1 Electromagnetic Waves

The propagation of an EMW consists of two components: a harmonically oscillating electric and magnetic field that are orthogonal to one another in space and in-phase in time. In free space (i.e. vacuum) the phase front of this field propagates forward at the speed of light $c \approx 3 \times 10^8$ m/s. The frequency of oscillation of the electric/magnetic fields is often denoted f and given in Hz. Using these two values one can define the wavelength (λ) of an electromagnetic wave – the distance over which one oscillation occurs – via the relation $c = \lambda f$. The wavelength is often a very useful parameter when visualizing electromagnetic interactions as this denotes the *size* of the wave. Typically, electromagnetic waves interact most strongly with structures that have characteristic dimensions on the order of the size of the wavelength (for instance, linear dipole antennas are often designed to have a length of $\lambda/2$).

In many cases, electric interactions dominate the way an EMW interacts with objects and as such it is often enough to only consider this component of the wave (this will be assumed for the rest of the thesis). Mathematically, a propagating electric field oscillation (henceforth referred so simply as an EMW or light) can be described by: $E_0 \cos(\omega t - kr + \phi)$, where E_0 is the maximum electric field amplitude, t is time, r denotes distance (this wave travels in the \hat{r} direction), and ϕ is a phase offset. The values $\omega = 2\pi f$ and $k = 2\pi/\lambda$ are the angular frequency and wavevector respectively. Often it is mathematically convenient to represent this wave in complex notation, i.e. $E_0 \exp(i[\omega t - kr + \phi])$ where the electric field oscillation is given by the real part of this expression. The description given here is known as a linearly polarized *plane wave* and is a very useful concept in studying electromagnetic interactions. The term “linearly polarized” simply implies that the electric field oscillates strictly along one spatial axis – while this is not required in general, for the purposes of this thesis it will suffice to restrict our discussion to this type of electromagnetic waves.

2.1.2 Permittivity and Refractive Index

When light propagates through a bulk material, as opposed to in free space, the propagation of the EMW is affected by interactions with the constituent atoms of the material. As an EMW passes over the atoms of a medium the charged electrons are perturbed in response to the electric field imposed by the wave. The perturbation of the electrons by the oscillating electric field results in oscillating charges which themselves re-emit (i.e. scatter) light

isotropically in the plane perpendicular to the polarization of the EMW. For a bulk medium where the impact of any single atom is negligible, the net effect is a secondary EMW with the same frequency but where the amplitude and phase delay (with respect to the incident wave) are determined by the *permittivity* of the material.¹ The superposition of the secondary and incident wave determines the net field within a medium.

The permittivity (ϵ) of a material is defined by the ratio of the electric displacement field amplitude (D) induced in the material and the incident electric field amplitude, i.e. $\epsilon = \epsilon_r \epsilon_0 = D/E$, here ϵ_0 is the permittivity of free space (a universal constant) and ϵ_r is the relative permittivity of the material. In principle the relative permittivity depends on the frequency of the EMW however for most dielectrics it is approximately constant at optical frequencies (in section 2.1.4 I will explore the case where this is not true). The relative permittivity is a complex number where the real part is related to the energy stored within the medium, while the imaginary part describes energy dissipation.²

In terms of optical propagation, it is often more intuitive to consider the refractive index of the material which is defined by $n = \sqrt{\epsilon_r}$. The refractive index, which is also complex valued, is useful in renormalizing the speed of propagation ($v = c/n$) and wavelength ($\lambda = \lambda_0/n$) of the propagating light. If the real part of the refractive index is very large, then the effective speed of propagation is significantly reduced – this corresponds to a secondary wave that lags the incident wave by nearly $\pi/2$ causing retardation of the total wave with respect to the incident wave. If the imaginary component of the refractive index is large then the wave is significantly attenuated/absorbed in the medium – corresponding to a secondary wave that is π out of phase with the incident wave, i.e. causing deconstructive interference.

2.1.3 Interaction Between an EMW and a Small Dielectric Sphere

Here I describe how a propagating plane EMW interacts with a *small* particle (as opposed to a homogeneous medium). The presence of a particle acts as a local inhomogeneity in the optical properties of the medium, and as a result a wave that would otherwise travel unperturbed will interact with this particle. Depending on the material and morphological properties of the particle these interactions will result in light either being scattered back into the medium, or absorbed by the particle itself resulting in heat generation.

The condition for a particle to be “small” is that its diameter or characteristic length is much smaller than the wavelength of light. This is known as the Rayleigh regime. By restricting the size of the particle to be deeply subwavelength the electric field across the particle is essentially uniform and a quasi-static approximation can be used. Here we will focus on the interaction of a plane wave with a small dielectric sphere because of the

availability of analytic solutions to the problem. This subsection largely serves as a prelude to the following section on plasmonics where we will see how the interaction with light can be strongly enhanced due to frequency dependent permittivity of noble metals at optical frequencies.

Consider a small dielectric sphere illuminated by linearly polarized monochromatic light of wavelength λ . If the diameter of the sphere is much smaller than the wavelength then at any moment the particle experiences an approximately uniform electric field and the interaction is effectively electrostatic in nature (Rayleigh approximation). The sphere becomes polarized in response to the applied electric field which causes the particle to act as a dipole. The dipole moment of the sphere is given by³:

$$p = \alpha E_0 \quad \text{where} \quad \alpha = 4\pi\epsilon_m a^3 \left(\frac{\epsilon_p - \epsilon_m}{\epsilon_p + 2\epsilon_m} \right)$$

here, p is the dipole moment induced in a sphere of radius a under an external electric field amplitude E_0 . The term α is the polarizability of the sphere and ϵ_p , ϵ_m are the permittivity of the particle and the surrounding medium respectively. Because the external electric field oscillates in a sinusoidal fashion, so too will the dipole moment of the sphere.

The interaction between light and particle are often characterized by *cross sections*. Optical cross sections are proportionality factors that relate the incident EMW intensity to the electromagnetic power lost to a certain decay pathway. Meanwhile light that is *not* lost to a decay pathway will continue propagation along the initial trajectory. The dominant decay pathways in light-matter interaction are scattering and absorption (their sum is known as extinction). The scattering cross section therefore determines the power of the light scattered by the particle while the absorption cross section determines the amount of power absorbed by the particle. In the quasi-static limit the cross sections for a spherical particle are given by:⁴

$$P_{\text{scattered}} = \sigma_{\text{scattered}} I_0 \quad \text{and} \quad P_{\text{absorbed}} = \sigma_{\text{absorbed}} I_0$$

$$\sigma_{\text{scattered}} = \frac{k^4}{6\pi} |\alpha|^2 = \frac{8\pi}{3} k^4 \epsilon_m^2 a^6 \left| \frac{\epsilon_p - \epsilon_m}{\epsilon_p + 2\epsilon_m} \right|^2 \propto V^2$$

$$\sigma_{\text{absorption}} = k \text{Im}\{\alpha\} = 4\pi k \epsilon_m a^3 \text{Im} \left\{ \frac{\epsilon_p - \epsilon_m}{\epsilon_p + 2\epsilon_m} \right\} \propto V$$

$$\sigma_{\text{extinction}} = \sigma_{\text{scattering}} + \sigma_{\text{absorption}}$$

where V is the volume of the sphere and ϵ_p , ϵ_m are the permittivity of the particle and the surrounding medium respectively. As can be seen from the

above, since the scattering cross section has a quadratic dependence on volume while the extinction cross section has linear dependence, for very small particles absorption tends to be dominant and approximately equal to extinction; however, for most dielectric particles where the permittivity is only moderately different than the host medium, both effects are often very small.

2.1.4 Localized Surface Plasmon Resonances

While for dielectric materials the optical properties are often constant in the visible regime this is not true for noble metals. Gold is an advantageous material in many systems due to its inert chemical properties and additionally shows a strong dispersion in its optical properties at visible wavelengths – the relative permittivity and refractive index for gold are shown in Figure 1a,b below. From looking at the optical cross section equations given above, when the real part of a materials permittivity is negative two times that of the host medium, the optical cross sections increase significantly. For gold, this resonance condition occurs just above 500 nm. In Figure 1c we can see the optical cross sections for a 50 nm gold sphere surrounded by water. As seen here, the absorption cross section is several times larger than the physical cross section at resonance.

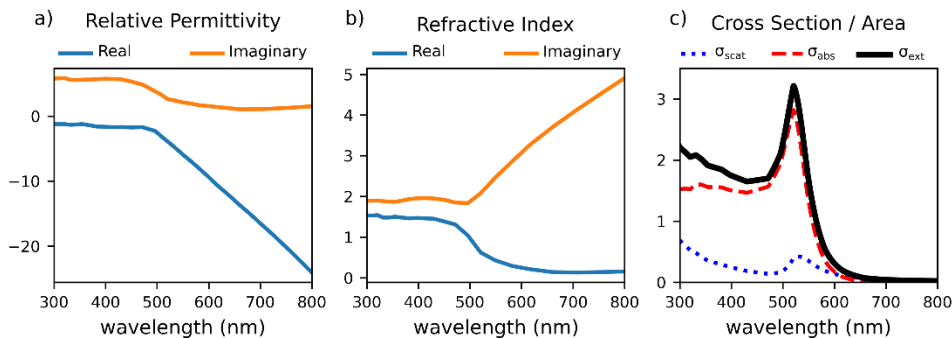


Figure 1 Optical properties of a gold particle. Bulk material properties of gold for a) relative permittivity and b) refractive index. c) Optical cross section for a 50nm gold sphere in water. Cross sections have been normalized by the physical cross-sectional area of the gold sphere.

Physically, the resonance occurs because of oscillations in the free electrons within the metal nanoparticle – known as a localized surface plasmon resonance (LSPR). This resonance causes plasmonic particles to act as an optical antenna where the plasmonic particle supports greatly enhanced electric fields that are tightly confined near the surface. Because of the increased light-matter interaction and electric field confinement due to LSPRs researchers use noble metal nanoparticles as an optical transducer to interact with matter on the nanoscale – something that has traditionally been difficult with conventional far field optics. Within the electrostatic (Rayleigh) limit, it can be shown that for a plasmonic sphere, the plasmonic electric field enhancement scales according to⁴:

$$\frac{|E_{\max}|}{|E_0|} \propto \left| \frac{\epsilon_p - \epsilon_m}{\epsilon_p + 2\epsilon_m} \right|$$

where E_{\max} is the maximum electric field, and E_0 is the incident electric field.

In addition to the enhanced electric fields, there has also been recent interest in using plasmonic particles as highly localized heat sources – a field known as thermoplasmonics. This field is intriguing since for small metallic nanoparticles often the absorption tends to dominate the extinction and therefore significant amounts of heat can be generated very locally. In the next section I will explore how this heat dissipation affects the surrounding environment.

2.2 Thermoplasmonics

This section will provide a basic understanding of the dominant processes involved in heat transfer with respect to plasmonic particles. When plasmonic particles are excited by electromagnetic radiation, their free electrons begin to oscillate which drives a current through the particle. Because the electrical resistivity of most plasmonic metals (e.g. gold) becomes non-negligible at optical frequencies, this leads to significant heat generation. The heat source density (q) that arises due to these oscillating currents is the product between the electric current flux (\vec{J}) and the local electric field (\vec{E}) within the particle, i.e.:

$$q(\vec{r}, t) = \vec{J}(\vec{r}, t) \cdot \vec{E}(\vec{r}, t)$$

Because all relevant thermal process in continuous wave illumination happened on a much slower time scale than the oscillations of the electric field, a more relevant parameter is the heat source density averaged over the period of the electromagnetic wave⁵ (see Figure 2 for an illustration of the internal heat source density of a gold bowtie nanoantenna):

$$q(\vec{r}) = \frac{\omega}{2} \epsilon_0 \text{Im}\{\epsilon_r(\omega)\} |\vec{E}(\vec{r})|^2$$

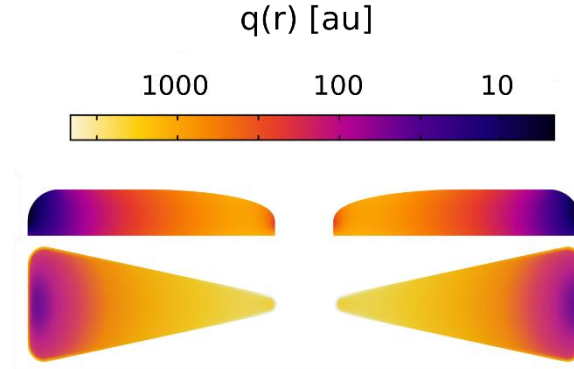


Figure 2 internal heat source density for optically excited plasmonic bowtie antenna. Shown here is the internal heat source density for a gold antenna that is optically excited with linear polarized light, where the electric field points along the long-axis of the antenna.

For most relevant plasmonic systems, the thermal conductivity of plasmonic material is orders of magnitude greater than the surrounding medium. As will be shown later, this results in a nearly constant internal temperature and the limiting factor determining the temperature profile is the thermal conductivity of the surroundings. As a result, often the most important parameter is the *total* heat dissipated within the plasmonic structure, rather than its distribution (this is only strictly true for low aspect ratio plasmonic structures). The total heat dissipated within the plasmonic structure (Q) is simply the integral of the heat source density over the volume of the plasmonic structure. The integrated dissipated heat is equivalent to the absorbed power as described by the absorption cross-section introduced in the previous section ($Q = P_{\text{absorbed}} = \sigma_{\text{absorption}} I_0$).

Heat Dissipation. For macroscopic objects there are typically two main pathways by which heat is dissipated into the environment: conduction and convection. Conduction occurs by the direct collision of adjacent atoms which therefore propagates the thermal energy from one atom to another – this is the process that occurs when the outside of a coffee mug gets hot due to the warm liquid on the inside. Convection on the other hand occurs when there is a fluid flow across a heated interface – i.e. when you blow on your hand to cool it down after a burn. In *most* thermoplasmonic systems heat transfer by conduction is typically dominant and convection can be neglected.⁶ Therefore, the remainder of this section will be devoted to studying heat transfer by conduction in thermoplasmonic systems.

The defining equation for conductive heat transfer is the Fourier heat equation:

$$\rho c_p \partial_t T - \kappa \nabla^2 T = q(r, t)$$

here, ρ is the local material density, c_p is the heat capacity at constant pressure, and κ is the thermal conductivity (note, this form of the equation assumes constant material properties). The first two terms (ρ and c_p) describe how much stored thermal energy is required to increase the temperature of a

material, while κ is a measure of how easily heat can propagate through a region. Using the above equation, and the relevant boundary conditions at any material interfaces, the temperature profile resulting from conductive heat transfer can be determined. In general, for complex systems the heat equation must be solved numerically to obtain meaningful results; however, for a spherically symmetric case an analytic solutions exists. For that reason, the remainder of this section will be devoted to analysing the case of a uniformly heated spherical gold particle in a homogeneous (water) medium, but the qualitative nature of these results can be readily extrapolated to many relevant systems.

2.2.1 Steady-state

I will first analyse the temperature profile due to steady state heating, i.e. where all properties are constant in time. For a gold sphere of radius a and with constant internal heat source density, within a homogenous water medium where no heat is absorbed, the Fourier heat equation reduces to:

$$-\kappa\nabla^2T = q \quad \forall r \leq a$$

$$\nabla^2T = 0 \quad \forall r > a$$

Here, the boundary conditions are⁷:

- Temperature increase at infinity is 0: $\Delta T(r = \infty) = 0$
- The temperature on opposite sides of a material interface are equal: $T(r^-) = T(r^+)$
- The heat flux through a boundary is equal to negative the product of the material thermal conductivity and the spatial temperature derivative: $J_q = -\kappa^+ \partial_r T^+$

Using the above equations, the temperature increase due to heating of the plasmonic gold sphere is given by:

$$\Delta T(r) = \frac{Q}{4\pi\kappa_m a} \left[1 + \frac{\kappa_m}{2\kappa_p} \left(1 - \frac{r^2}{a^2} \right) \right] \quad \forall r \leq a$$

$$\Delta T(r) = \frac{Q}{4\pi\kappa_m r} \quad \forall r > a$$

where κ_m and κ_p are the thermal conductivity of the medium (e.g. water) and particle (e.g. gold) respectively – note: the subscripts m and p will be used to describe either the properties of the medium or the particle for the remainder of this section. Notice that since $\kappa_p \gg \kappa_m$ for gold in water, the term in brackets for the temperature profile within the gold sphere is approximately 1 and therefore the internal temperature is nearly constant. The radial

temperature profile for a heated sphere is shown below in Figure 3. It is interesting to note that outside the sphere the temperature profile is the same as for an infinitesimal heat source in a uniform medium with the same integrated total heat deposited.

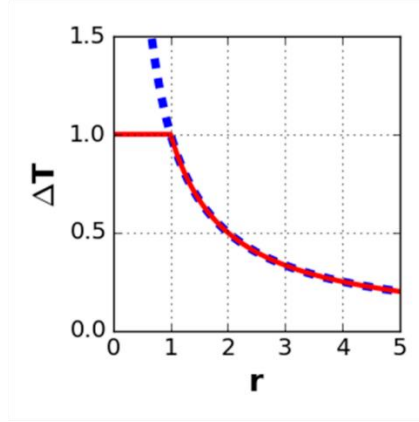


Figure 3 Steady state heating profile. Shown above is the steady state heating profile for a point source (dashed blue line), and for a gold sphere in water (red solid line) for the same total heat dissipation. Temperature increases have been normalized to the surface temperature of the sphere and distanced normalized to the radius of the sphere.

Collective Effects. The results for single gold sphere in a uniform medium can easily be extended to the case of a collection of gold spheres. For a relatively low density of plasmonic particles (spheres) the temperature in the surrounding medium can simply be taken as the sum of the contributions from each individual gold sphere, i.e.:

$$\Delta T(\vec{r}) = \sum_i \frac{Q_i}{4\pi\kappa_m|\vec{r} - \vec{r}_i|}$$

While the individual spheres under this approximation heat up their surroundings the same as in the case of an isolated sphere, their collective effects can cause a much larger volume of the surroundings to be effectively heated. In many cases, it is often the aggregate diameter of the collection of individual spheres that determines the temperature decay profile.⁵ In Figure 4 we can see how different planar arrangements of gold nanosphere can change the overall temperature distribution in the surrounding medium.

Theory

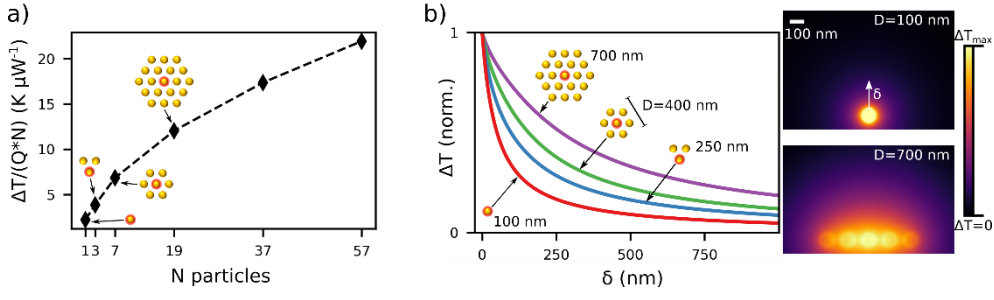


Figure 4 Temperature increase and profile due to collective heating. Temperature increase for collections of gold spheres with 100 nm diameter, and 50 nm edge-to-edge spacing. a) Temperature increase of different collections of uniformly heated gold spheres where the temperature is taken 10 nm from the surface of the central gold sphere (indicated in red), perpendicular to the plane of spheres. Temperature increases are normalized by the total power dissipated by the collection with each individual sphere dissipating the same amount. b) Shown here are the normalized temperature profiles for different planar arrangements of uniformly heated gold spheres. Left: Temperature decay curves extending normally away from the central gold sphere normalized to the maximum temperature in the system. Right: Temperature maps for the smallest planar arrangement (single sphere) and for the largest (19 spheres). Temperature maps are from a plane orthogonal to the plane of the particles.

While I have thus far restricted the discussion to the case of a gold sphere in a homogeneous medium, often a much more relevant scenario is a gold particle at an interface. Often, an approximation is taken where the average thermal conductivity of the surroundings is used.⁸ This approximation is often only valid if the plasmonic structure extends further along the interface than away from it and if the thermal conductivities of the two mediums which form the interface are not drastically different. In the case where the thermal conductivities of the two mediums *are* very different, it can often be more useful to take the average of the thermal conductivities weighted by the percentage of the particle's surface area in contact with that medium when trying to obtain the temperature increase of the plasmonic structure.

2.2.2 Temporal Dynamics

In the steady-state regime the thermal conductivity is the most important parameter which dictates the temperature profile; however, for transient temperature profiles the thermal diffusivity ($D = \kappa / \rho c_p$) tends to be more important. Here I will examine two relevant cases of transient temperature evolution in our model system: the temperature increase/decrease in response to a step-wise change in heating power and the temperature response due to harmonic heating.

Temperature Evolution. It has been found that the temperature evolution outside the sphere following a stepwise change in heating power (i.e. laser turned on or off within the context of thermoplasmonics) can be well approximated with the following equations⁵:

$$\text{on: } Q(t) = Q_0 \quad \forall t > 0 \quad \rightarrow \quad \Delta T(r, t) = \frac{Q_0}{4\pi\kappa_m r} [1 - \text{erf}(\sqrt{t/\tau})]$$

$$\text{off: } Q(t) = Q_0 \quad \forall t < 0 \quad \rightarrow \quad \Delta T(r, t) = \frac{Q_0}{4\pi\kappa_m r} \text{erf}(\sqrt{t/\tau})$$

where $\tau = r^2/4D_m$. The most interesting observation at this point is that the time constant of the temperature evolution is a function of the distance away from the heat source. This results from the fact that at larger distances a greater volume must be heated up. Shown below in Figure 5 is the temperature evolution around a heated gold sphere for the “on” case, as well as how the temperature evolution time constant changes in water with distance from the location of the heat source. Note that while the time constant increases significantly at larger distances, the total temperature increase is also significantly reduced so the “impact” of this slower response is less pronounced.

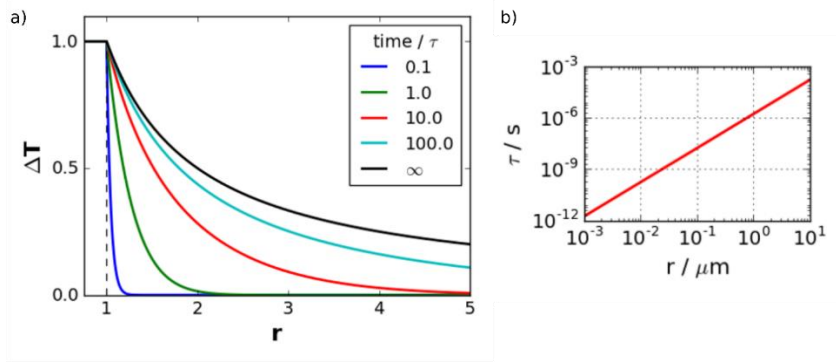


Figure 5 Transient evolution of temperature profile around a single gold sphere. a) Temperature profile after stepwise heating of a gold sphere in water at different times (normalized to time constant at $r=a$). Temperature is normalized to the temperature of the sphere and distance is normalized to the radius of the sphere. b) Time constant for temperature evolution in water as a function of distance.

Harmonic Heating. For harmonic heating we can immediately identify two limiting regimes. In the low frequency case, the temperature profile will follow that of the heating modulation. In the high frequency case the finite thermal response time of the system will not permit significant temperature fluctuations and therefore only the time averaged deposited heat is relevant (the system is essentially under steady state conditions). In between these two regimes there is varying degrees of dampening of temperature modulations. If we assume that the heat source density is modulated according to $Q(t) = Q_0(1 + \cos(\omega_{\text{mod}}t))$ then the temperature increase outside of the spherical particle is given by⁹:

$$\Delta T(r, t) = \frac{Q_0}{4\pi\kappa_m r} \left[1 + \text{Re} \left\{ \frac{\exp(ik_{\text{th}}(r - a) - i\omega_{\text{mod}}t)}{1 - ik_{\text{th}}a - i\omega_{\text{mod}}\tau_{\text{NP}}} \right\} \right]$$

where $k_{\text{th}} = (1 + i)\sqrt{\omega_{\text{mod}}/2D_s}$ describes the dampening of the temperature oscillations and $\tau_{\text{NP}} = a^2\rho_p c_{\text{pp}}/3k_m$ is a time constant for the thermal fluctuations of the particle. In Figure 6 we can see how the temperature profile around a 50 nm diameter gold sphere in water is affected for different modulation frequencies. Notice that at 1 GHz nearly all thermal modulation is damped, this explains why the oscillations in current due to the

Theory

oscillating electromagnetic (≈ 100 THz) field can be ignored as mentioned at the beginning of this section.

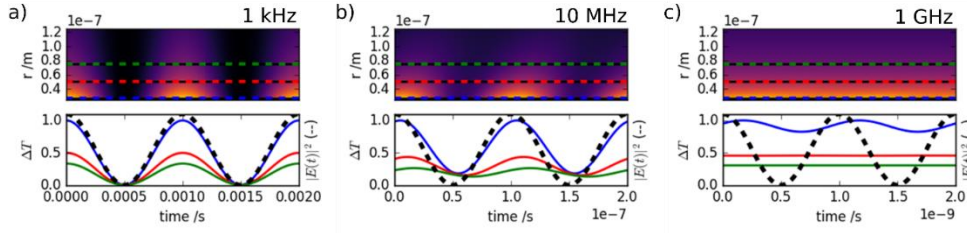


Figure 6 Harmonic heating of a single gold sphere (diameter = 50 nm). Top row: Radial temperature maps vs time at different modulation frequencies. Bottom row: Temperature curves vs time at different modulation frequencies for discrete radial distances. Radial distances correspond to dashed lines in top row. Dashed black line is the heating modulation profile. Modulation frequencies are 1 kHz, 10 MHz, and 1 GHz for a), b), and c) respectively.

Similar to how the steady state temperature profile for a collection of particles can be determined as the sum of contributions from each individual particle, the harmonic temperature profile from multiple particles can also be calculated. Shown in Figure 7 is the effective degree of modulation at varying distances from a linear array of gold spheres under harmonic heating. Although in this case the individual spheres are the same size as in Figure 6, the temperature modulations are significantly damped at lower frequencies for a long linear array. In general, it is the characteristic length scale of the meta-structure which dictates the maximum effective modulation rate.

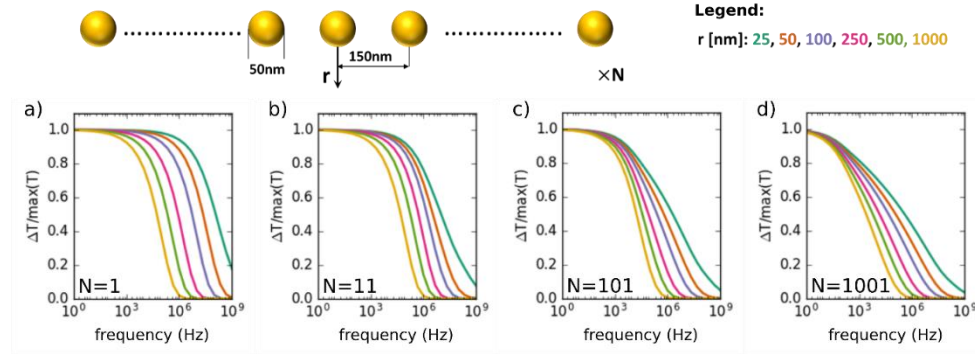


Figure 7 Harmonic heating for linear arrangements of gold particles in water. Extent of temperature modulation for various distances from a line of gold particles vs modulation frequency. a), b), c), and d) correspond to linear arrangements of 1, 11, 101, and 1001 particles respectively with the parameters/spacing shown at the top left. Coloured lines correspond to distances given by legend in top right.

2.3 Thermophoresis

It is well known that colloidal particles tend to experience a drift velocity when placed in an external temperature gradient.¹⁰ This tendency towards directed motion is given by the simple equation

$$\vec{v}_{\text{drift}} = -D_T \nabla T$$

where ∇T is the local temperature gradient and D_T is known as the thermal diffusion coefficient (or more correctly, the thermophoretic mobility). The magnitude of D_T has been experimentally observed to fall within the limited range of 10^{-8} to 10^{-7} $\text{cm}^2\text{s}^{-1}\text{K}^{-1}$ in many cases¹⁰ although the exact value is highly system specific and can be positive or negative depending on the salinity of the solvent.¹¹ For colloidal dispersions with a relatively low concentration (such that interparticle interactions can be safely neglected) the thermally induced particle flux (J_{thermal}) will be opposed by a diffusive particle flux ($J_{\text{diffusive}}$) which opposes the concentration gradient, i.e.

$$J_{\text{net}} = J_{\text{thermal}} + J_{\text{diffusive}} = -cD_T\nabla T - D\nabla c$$

where c is the local concentration of colloidal particles, and D is the diffusion coefficient of the colloids. Under steady state conditions the net particle flux must be zero and the local relative colloid concentration due to a local temperature change ΔT is given by¹²

$$\frac{c}{c_0} = \exp\left(-\frac{D_T}{D}\Delta T\right)$$

The ratio between the thermophoretic mobility and the diffusion coefficient is often referred to as the Soret coefficient (S_T) and is the parameter that determines the extent of depletion or accumulation that occurs for colloidal particles due to a temperature gradient. The thermophoretic mobility is generally viewed as insensitive to particle size^{13–15} and depends mainly on the specific interactions at the particle/solvent interface. However, while the thermophoretic mobility is independent on the particle size, the Soret coefficient shows a linear dependence due to the inverse dependence of the diffusion coefficient on particle radius (for spherical particles under the Stokes drag approximation). As a result, the size of the colloid will significantly impact the extent of depletion/accumulation due to thermophoretic effects resulting from the increased (decreased) Brownian motion for smaller (larger) particles.

Physical Mechanisms. Part of the reason for the highly system specific values for D_T stems from the multiple physical mechanisms which gives rise to thermophoretic motion. Arguably the most fundamental mechanism for thermophoresis results from thermo-osmotic flows at the particle/solvent interface. This interfacial flow arises due to thermally induced inhomogeneities in the electric double layer surrounding the colloid.¹⁶ The counterion cloud adjacent to the charged surface of a colloid is in local equilibrium and follows a Poisson-Boltzmann concentration distribution which is temperature dependent. Therefore, the thermal gradient induces a concentration gradient of counterions across the particles surface which creates an osmotic pressure imbalance (Figure 8a). This pressure imbalance causes the surrounding liquid to flow towards the hot side of the colloid.

Because of this interfacial fluid flow, the colloid will move with the same velocity but in the opposite direction, i.e. against the temperature gradient towards cooler temperatures (Figure 8c).

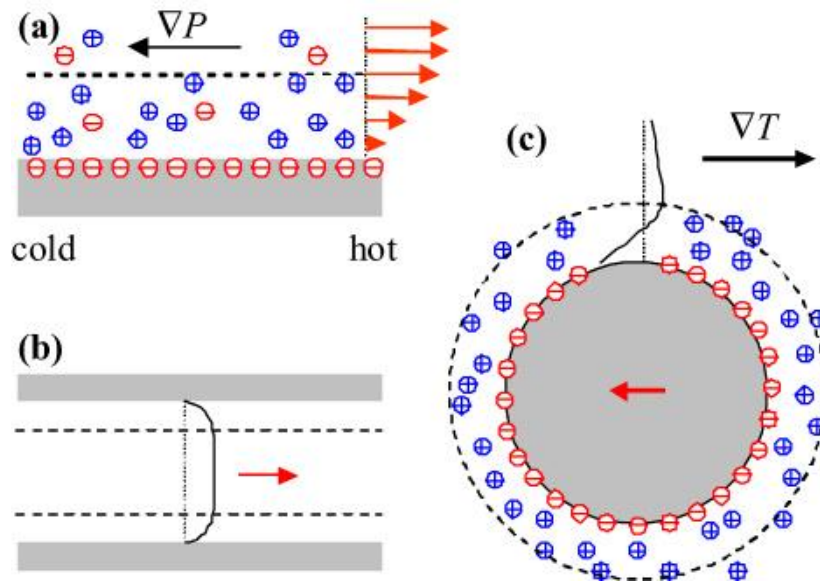


Figure 8 Thermo-osmotic flows due to temperature gradient. a) Thermo-osmotic flow near a charged surface under a temperature gradient. b) Analogous case of thermo-osmotic flows in a microchannel. c) Thermo-osmotic flows around a charged colloidal sphere cause the particle to drift in the opposite direction as the temperature gradient. Solid black line shows the fluid velocity profile in the laboratory frame of reference. Reprinted with permission from¹⁶. Copyright 2010 IOP Publishing. All rights reserved.

Another contribution to thermophoretic motion is due to the temperature dependent density of most solvents. Typically, liquids will decrease in density at elevated temperatures. As outlined by Würger, van der Waals interactions are typically dominant for colloidal particles in many liquids. As a result, the colloidal particle will be more strongly attracted to regions of higher liquid density which occur at lower temperatures (Figure 9).¹⁶ Due to the stronger attraction on the cold side, there tends to be a net solvent flow along the colloid/solvent interface towards higher temperatures, again resulting in colloidal motion towards lower temperature regions. It is interesting to note that the thermophoretic mobility of many colloidal particles in water changes sign (i.e. thermophobic to thermophilic) at around 5 °C, which is also the temperature where water density is at a maximum.¹⁷ This tendency for particles to migrate towards regions of high solvent density further illustrates why, for many systems, colloidal particle motion is typically thermophobic.

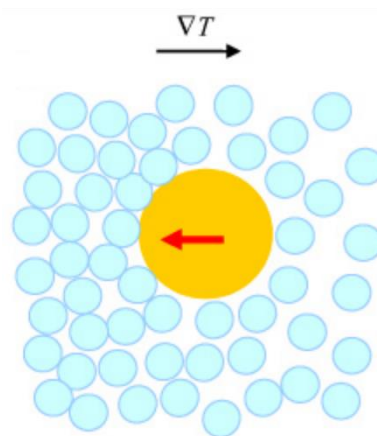


Figure 9 Density driven thermophoresis. A colloidal particle where the surrounding liquid has a temperature dependent density with higher densities at lower temperatures. Dispersion forces attract the colloid towards the cold side (regions of higher density). Reprinted with permission from¹⁶. Copyright 2010 IOP Publishing. All rights reserved.

From the thermophoretic mechanisms described above, it would appear that colloidal particles always exhibit thermophobic behaviour ($D_T > 0$). While thermophobic behaviour of particles is often observed, controlling the properties of the solvent can have a dramatic effect on the magnitude of the thermophoretic mobility and even cause sign reversal ($D_T < 0$) creating thermophilic behaviour. Putnam and Cahill have observed that for solutions with high salt concentrations, the thermophoretic mobility could be changed over an exceedingly large range ($-0.9 \times 10^{-7} < D_T < 1.5 \times 10^{-7}$ [cm^2/sK]) by changing the type of dissolved ions.¹¹ This interesting result can be understood by considering the motion of the dissolved ions in response to a thermal gradient. In addition to the intrinsic thermophoretic motion of the colloid, dissolved ions will also respond in a similar fashion. The thermophoretic motion of the dissolved ions (which can vary in magnitude as well as sign) results in ionic concentration gradients thereby creating a macroscopic electric potential. This thermophoretic response of the ionic solution thus induces electrophoretic motion of the colloidal particle under study.¹⁶ Depending on the surface properties of the colloid and the ionic concentration of the solvent (including the ionic species), thermophoretically induced electrophoresis of the colloid can dominate the overall thermophoretic motion and generate either thermophilic or thermophobic motion of the colloids under study. An illustration of a technique to generate a thermophilic response for a target particle is shown in Figure 10 below.

Theory

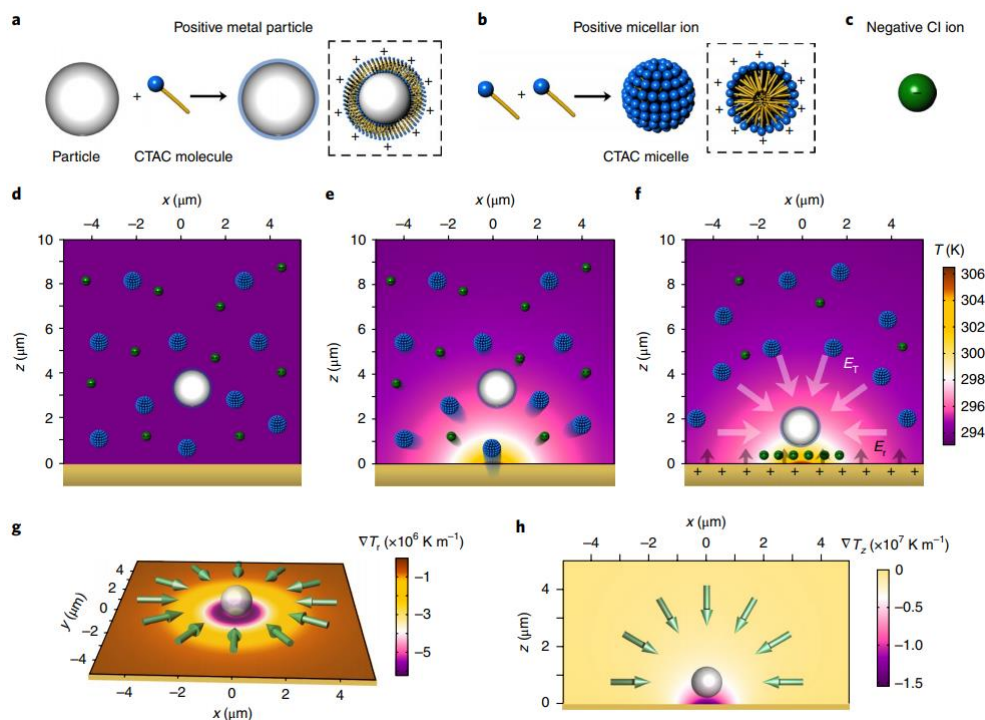


Figure 10 Creating a thermophilic response for a target particle. a) Target particle undergoes surface modification to generate a positive surface charge. b, c) Counterions for the system – b large positive micellar counterions, c small negative Cl counterions. d) Dispersion of target particle and counterions in solution. e) Optical heating creates a temperature gradient, counterions thermophoretically move in response to this gradient. f) Thermophoretically induced counterion concentration gradient creates a standing electric field. This electric field points towards regions of higher temperature causing the positive target molecule to electrophoretically move to the high temperature region. g,h) Simulated temperature gradient and corresponding electrophoretic force direction for in-plane and out-of-plane respectively. Reproduced with permission from¹⁸. Copyright 2018, Springer Nature.

Applications. One field where the utilization of thermophoretic effects shows great promise is quantifying biomolecular interactions¹⁹. Because the thermophoretic mobility for complex molecules (such as proteins) is highly sensitive to molecular properties such as the size, charge, hydration shell or conformation, the technique of microscale thermophoresis can be used to measure changes in the thermophoretic depletion that occurs because of interparticle binding. This is especially advantageous for small molecule interactions where the net mass of the product molecule is similar to the initial target molecule; this contrasts with more established techniques such as surface plasmon resonance (SPR) sensing which require significant mass change to observe a detectable signal. Microscale thermophoresis has demonstrated applications in studies such as protein binding assays and can be performed in free solution (as opposed to on a surface as in SPR).^{20,21}

Thermophoretic forces have also been demonstrated as a means by which a force can be imparted on a particle to induce motion or localize the position of the particle. This type of experiment is analogous to plasmonic optical trapping – where optical forces act on a particle – but instead utilizes a temperature gradient to establish the trapping potential well. These types of traps can utilize the inherent thermophobic response of most particles by creating a local temperature minimum with dynamic temperature fields.^{22,23}

Alternatively, the systems can be engineered to illicit a thermophilic response of the target molecule by tailoring the salinity of the solution (as shown in Figure 10).^{18,24} In addition to creating forces with an external temperature field, by utilizing a heterogeneous structure (i.e. half the particle generates heat) the particles themselves can establish a temperature gradient to thermally induce their own motion creating self-propelled particles.²⁵⁻²⁷

2.4 Thermoplasmonic Bubbles

The ability to introduce a phase change in solution via the formation of a bubble can be achieved by countless different means and with equally many applications. A full description of all such processes is beyond the scope of this text. Here, I endeavour only to elucidate the process of bubble nucleation, formation, and dissipation that occurs via thermoplasmonic means. I further restrict the discussion to bubble formation via continuous wave illumination, as opposed to high intensity pulsed illumination, as the physics and applications are quite different. This restricted domain of continuous wave thermoplasmonic bubbles and their applications also has the advantage of being a topic which is currently of significant interest to the scientific community and has only recently begun to be studied in detail.

Thermoplasmonic Micro-Bubble Nucleation, Growth, and Dissipation.

Much of what we know about the dynamics of thermoplasmonic bubbles comes from recent studies focused on the nucleation, growth, and subsequent dissipation of microbubbles. These systems typically involve regular arrays of plasmonic particles, or continuous plasmonic films, which are illuminated by a heating laser that has been focused to a minimum diameter of several microns. In these cases, the heating laser focal spot size is the limiting factor for the extent of the heat source density and elevated temperatures extend significantly into the adjacent solvent. Previous studies on thermoplasmonic bubbles have been performed on systems involving plasmonic particles in water^{28,29}, as well as other solvents such as n-alkanes^{30,31}. Utilizing a solvent such as pentane instead of water can significantly reduce the boiling point and help prevent thermally induced damage to the plasmonic structure; however, the thermal and fluidic properties of these solvents differ significantly and very different bubble dynamics have been observed,³⁰ the following analysis is restricted to situations where only water is used as the solvent.

While we are typically accustomed to bubble formation at the boiling point of water, i.e. 100°C (such as when boiling water on the stove), this is not the case for nucleation of thermoplasmonic bubbles. While it is energetically favourable for H₂O to be in a gaseous state at temperatures above 100°C, there is still a considerable energy barrier that prohibits this transition without suitable nucleation sites already being present – e.g. pre-existing bubbles due to surface roughness. The absence of nucleation sites in most plasmonic

systems prohibits bubble formation at such a relatively low temperature. Conversely, there is an upper limit to the temperature at which a bubble can form, the spinodal temperature at $\approx 280^\circ\text{C}$ (assuming the system is at standard atmospheric pressure). At this temperature water vapor and liquid water are indistinguishable and above this temperature only wave vapor can be present. In between these two temperature extremes (boiling temperature and spinodal temperature) is the point at which bubble formation is observed to occur in thermoplasmonic systems – the kinetic spinodal temperature. At the kinetic spinodal temperature, random density fluctuations within the liquid cause the spontaneous nucleation of a bubble which will subsequently permit further growth.⁵ In 2014 Baffou et al. utilized temperature imaging via quadriwave shearing interferometry to directly observe the temperature at which bubble nucleation occurs.²⁹ In this work a regular array of closely spaced plasmonic nanoparticles was illuminated with a focused heating laser. The diameter of the focal spot was varied from 4.6 – 64 μm and in all cases bubble formation occurred at approximately 220°C (see Figure 11). The exact value of the temperature corresponding to bubble formation depends on several factors including the amount of dissolved gas within the solvent, with degassed water typically showing a much larger nucleation temperature than air-equilibrated water.^{32,33} Immediately following bubble nucleation, fast transient oscillations in the bubble diameter have sometimes been observed.³²

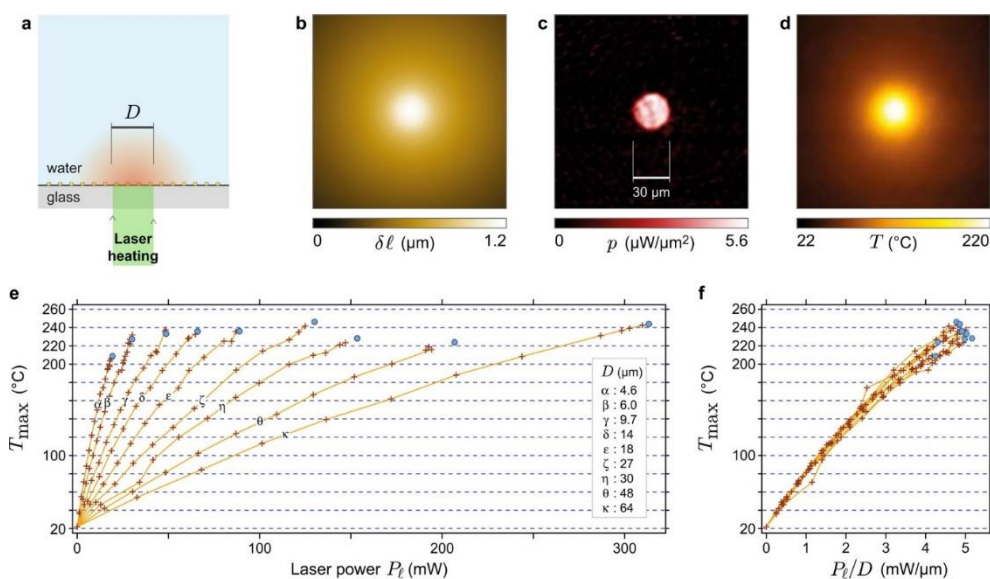


Figure 11 Bubble Nucleation Temperature. a) Illustration of experimental setup. b) Thermally induced optical path difference. c) Heat source density. d) Temperature profile – extracted from image c. e) Maximum temperature versus laser power for different laser beam focal diameters. f) Maximum temperature for all heating laser focal diameters as a function of the laser power scaled by the beam diameter. Reprinted with permission from²⁹. Copyright 2014 American Chemical Society.

After the initial nucleation of a bubble, the subsequent growth has been observed to be dominated by two distinct phases: vaporization and diffusive growth. In 2017 Wang et al. used an ultra-high speed camera to directly monitor the growth of thermoplasmonic microbubbles in both degassed water and air-equilibrated water.²⁸ Here, a periodic array of closely spaced

plasmonic nanoparticles was illuminated with a heating laser which had been focused to a diameter of 10 μm at the nanoparticle plane. For both the degassed water as well as the air-equilibrated water the initial bubble growth was nearly identical. After some transition time, bubble growth in the degassed water essentially stopped while in the air-equilibrated water the bubble growth rate increased (see Figure 12). From this, the authors concluded that the initial bubble growth was dominated by direct vaporization of superheated water immediately adjacent to the illuminated plasmonic particles. The second phase of growth was determined to be due to diffusion of gas molecules from the superheated water into the bubble – explaining why only the bubbles in air-equilibrated water continued to grow. This diffusive growth is permitted because the solubility of air in water decreases with increasing temperature, therefore the heated water becomes supersaturated and the dissolved air will preferentially exist within the bubble. Due to the geometry of the bubble at the plasmonic array (i.e. solvent/substrate interface), part of the bubble/water interface tends to be in a heated/oversaturated region for an extended period, and as such diffusive bubble growth is nearly continuous. This situation contrasts with n-alkanes where the solubility of air tends to increase with increasing temperature which would prohibit this second phase of bubble growth further illustrating the contrast of these two systems³⁴. The self-limiting nature of bubble growth in degassed water has been reported on several occasions^{33,35} and in some cases can be used as an advantageous means by which bubble growth can be limited during continuous illumination of extended plasmonic arrays/films³⁶ – although in practice degassed water is often difficult to achieve and maintain.

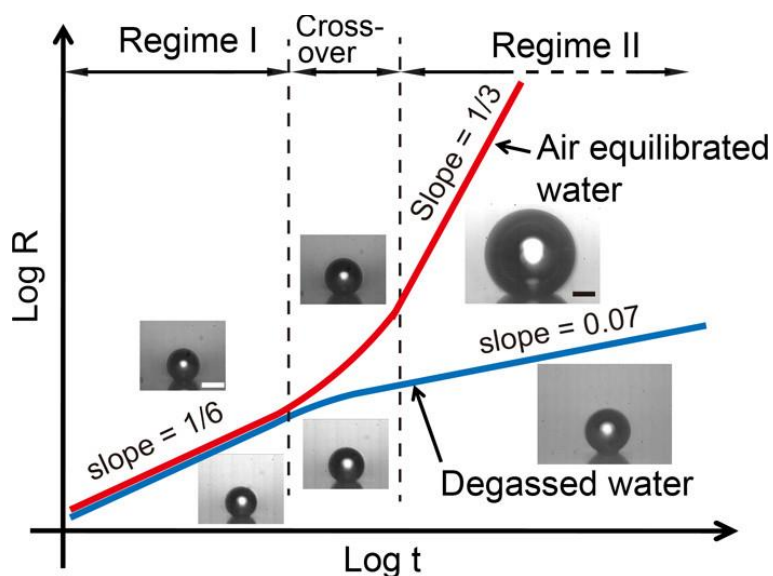


Figure 12 Thermoplasmonic bubble growth in air equilibrated water and degassed water. Presented here is an illustration showing the two regimes of sustained bubble growth, i.e. Regime I: vaporization, and Regime II: diffusive growth. Note that only bubbles in air equilibrated water grow at an appreciable rate from diffusion of oversaturated air molecules. Reprinted with permission ref²⁸. Copyright 2017 American Chemical Society.

Once the heating laser has been stopped the bubble is permitted to dissipate. For bubbles that are composed of a significant amount of dissolved gas (as opposed to solely water vapor), bubble dissipation tends to be extremely slow – often on the order of seconds to tens of minutes depending on the initial bubble size.²⁹ This slow dissipation is a result of the rate at which the gas can be reintroduced to the surrounding solvent. As the bubble dissipates the gas, the water immediately surrounding the bubble becomes oversaturated; therefore, the process is limited by the diffusion of the gas within the solvent away from the oversaturated region. The rate of bubble dissipation for the case of colloidal gas bubbles in a homogeneous solution has been solved analytically, showing a quadratic dependence of the bubble lifetime on the initial bubble size in the limit of large bubbles.³⁷ This quadratic dependence has been observed experimentally for large microbubbles supported by various types of continuous plasmonic structures.^{29,38} The dynamics of bubble dissipation for systems with large interparticle spacing for the plasmonic structures can be more complicated but follows a similar trend.³³ For the case of thermoplasmonic bubbles that are composed mainly of water vapor (i.e. formed within degassed water) the dissipation is much more rapid; however, it can still be on the order of several seconds, likely due to incomplete degassing and therefore some internal gas content.³⁵

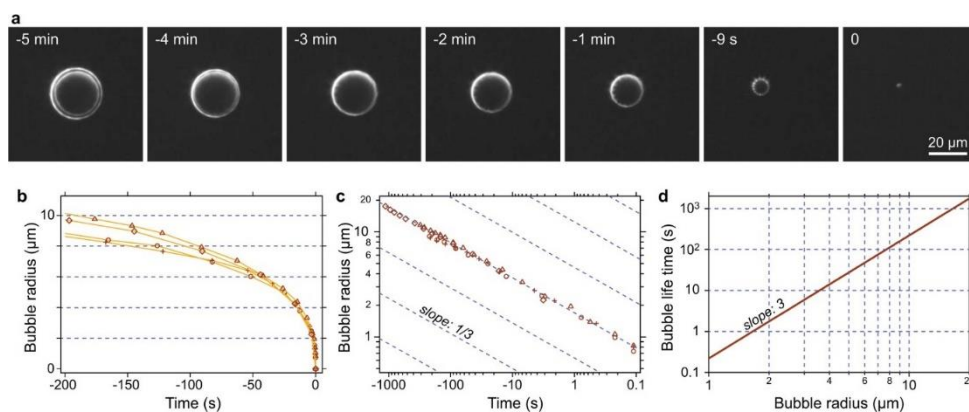


Figure 13 Bubble dissipation after heat source density turned off. a) Darkfield images of a microbubble during dissipation. b) bubble radius versus time for four different bubbles. c) Same data as image b but with log-log scaling. d) Bubble lifetime as a function of the initial bubble radius – fit to experimental data in images b and c. Reprinted with permission from²⁹. Copyright 2014 American Chemical Society.

Applications. Thermoplasmonic bubbles have previously been utilized as reconfigurable optical elements providing a means by which the optical response of a system can be addressed optically from the far-field, without requiring materials with intrinsically nonlinear optical properties. In 2013 Zhao et al. demonstrated how the formation of a bubble on a plasmonic waveguide could act as a reconfigurable lens.³⁹ In this work, an arc-shaped grating is used to couple incident 808 nm light into propagating SPPs. A second 405 nm laser is used to form a bubble adjacent to the grating coupler. The combination of the grating coupler with the bubble results in either divergence, collimation, or focusing of the propagating SPPs depending on the size of the bubble – which is itself controlled by the intensity of the 405

nm heating laser. In this way the authors could selectively configure the optical properties of their system by tuning the size of the thermoplasmonic bubble. In 2016 Gan et al. showed how the resonance of a metallic hole array could be widely tuned by the formation of a bubble.⁴⁰ By tuning the bubble size, the effective refractive index of the system can be controlled thereby changing the resonance frequency. This change in the resonance frequency of the structure was demonstrated to act as a dynamic filter for NIR light where the transmission intensity was strongly dependent on size of the plasmonic bubble.

One field where thermoplasmonic bubbles show perhaps the most promise is as active manipulation elements in microfluidic systems. Flow control via bubble formation has been demonstrated where the presence of a bubble can physically block fluid flow. This was demonstrated in 2011 by Zhang et al. where chromium pads were used to absorb 980 nm light to generate a bubble in a microfluidic channel.⁴¹ The presence of a bubble could then be used to block a microfluidic channel thereby acting as a valve providing far-field optical control of the microfluidic system. The authors also showed how the expansion or contraction of a bubble could itself induce fluid flow and act as a pump. This technique was extended to a fibre-optically controlled system in 2014 by Kim et al.; here, a fibreoptic microheater was created by the deposition of titanium on the tip of a fibre which was then attached to a microfluidic channel.⁴² Once again, the plasmonically enhanced absorption was used to thermally generate a bubble which could inhibit fluid flow.

Thermoplasmonic bubbles can also be used to actively generate flows within a microfluidic system via Marangoni convection. When a bubble is formed by generating heat with plasmonic structures on a substrate, there exists a temperature gradient across the surface of the bubble. Since the surface tension at the bubble-water interface is temperature dependent this creates a surface tension gradient which induces convective flows within the solution. Such flows have been experimentally observed from bubbles generated on gold films,⁴³ as well as around plasmonic nanoparticle clusters.⁴⁴ The ability for such flows to be utilized as extremely versatile active microfluidic controlled elements has been investigated by Namura et al., where they have found that by controlling the temperature gradient profile different flow patterns, including particle jets, could be formed,⁴⁵ and that by changing the solvent properties the flow can be suppressed or even reversed.⁴⁶ It is predicted theoretically that the Marangoni flow speeds should tend to increase as the bubble diameter decreases⁴⁷ with the ultimate limit being that of a point like force singularity known as a Stokeslet.⁴⁸ In 2017 it was shown that by limiting the bubble diameter to approximately 10 μm , extreme flow speeds approaching 1 m/s could be achieved.³⁶ These Marangoni flows have previously been demonstrated as a means of direct particle printing as particles in solution are driven by the flows and deposited at the intersection line where the bubble meets the substrate.^{49,50}

3 Experimental Methods

Provided here is a summary of the main experimental techniques that were utilized in the research that forms the basis of this thesis. These techniques were directly applied in appended papers I and II. A complete summary of the appended papers is given in Chapter 4; however, in short, the experimental methods of: plasmonic optical trapping (3.1.1), plasmonic anti-Stokes thermometry (3.2), and observation of thermophoresis (3.3) were used in appended paper I, while the method of observing plasmonic nano-bubbles (3.4) was used in appended paper II.

3.1 Optical Trapping

Optical trapping, first introduced by Arthur Ashkin in the 1970s, has become a ubiquitous tool in research labs worldwide.^{51,52} This technique is based on the fact that light carries momentum, and this momentum can be transferred to an illuminated object. To envision this momentum transfer and the associated force imagine a collimated beam of light that strikes a mirror at normal incidence along the $+\hat{x}$ direction. The light is perfectly reflected, so that it then travels along the $-\hat{x}$ direction. In this scenario, the incident light carries $+p\hat{x}$ momentum, while the reflected light carries $-p\hat{x}$ momentum; therefore, to conserve linear momentum a total of $+2p\hat{x}$ momentum must be transferred to the mirror. Although momentum is transferred, the associated force is incredibly small – for incident light with a total power of 1 mW only 7 pN of force acts upon the mirror⁵³. Because these forces are minute optical tweezers are relegated to only trapping very small objects (typically on the order of several microns or less).

The basic configuration used in optical trapping consists of a laser beam that is focused by a high numerical-aperture microscope objective. Dielectric particles will tend to experience a force which pulls them towards a point near the laser focus. To understand the principles of optical trapping we will start with the ray optics regime – i.e. where the trapped particle is much larger than the wavelength of light. In this regime all forces present can be understood by solving the Fresnel equations and applying conservations of linear momentum. There are two principle forces that exist in optical trapping: the scattering force and the gradient force. The scattering force is simple to understand, any light that is scattered (either reflected or scattered isotropically) by the object will cause the trapped particle to experience a force in the direction of the incident light (essentially the same situation as the mirror example provided above). The gradient force on the other hand is more complex. Qualitatively, the gradient force always pulls particles of higher refractive index than the surrounding medium to the region of highest electric field intensity (i.e. along the electric field intensity gradient). In the ray optics regime this can be understood with the help of Figure 14 below and by looking at how the light transmitted through the trapped particle behaves. Essentially, if a spherical particle is situated so that it is centred around the

laser focus than the symmetry of the system requires that the transmitted light carries the same momentum vector as the incident light and therefore no force is applied to the particle (Figure 14a). However, if the particle is not situated symmetrically around the laser beam focus, then the transmitted light will carry a different momentum vector than the incident light, and therefore the particle must feel a force opposite in direction to this change in momentum (Figure 14b-d).

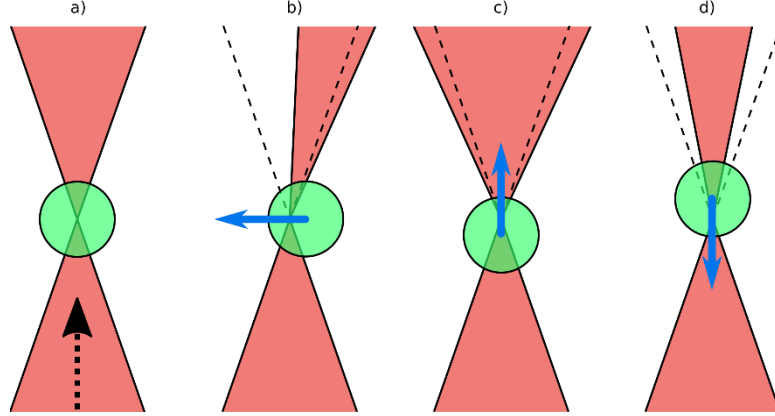


Figure 14 Illustration of gradient force in ray optics regime. Dashed black arrow indicates direction of light propagation, red area is the laser profile, green circle is the trapped dielectric sphere, and blue arrows indicate the direction of the applied gradient force. a) nominal case, particle centred around laser focal point – no force. b) Particle is offset from laser focus such that light is refracted to the right – applied force to the left. c) Particle is situated such that transmitted light is more divergent than incident light – applied force along propagation direction. d) Particle is situated such that transmitted light is less divergent than incident light – applied force is opposite propagation direction.

For very small particles, such that their characteristic length scale is much smaller than the wavelength of light, the ray optics picture cannot be used. Nonetheless the same principles still apply, and the particle will feel qualitatively similar scattering and gradient forces. Consider a small dielectric sphere illuminated by linearly polarized monochromatic light of wavelength λ . Using the formulism described in section 2.1.3, the power of the light which is scattered by the particle is given by $P_{\text{scattered}} = \sigma_{\text{scattering}} I_0$. Since this scattered light is radiated symmetrically it carries no net momentum; therefore, there is a net decrease in the momentum carried by light after interacting with the particle. Similarly, the power which is absorbed by the particle is given by $P_{\text{absorbed}} = \sigma_{\text{absorption}} I_0$, which similarly carries no net momentum.

Conservation of momentum thus requires there to be a force acting on the particle which is proportional to the power not transmitted by the particle. This force is known as the radiation pressure and describes how the absorbed and scattered light *pushes* the particle along the axis of propagation i.e. $F_{\text{radiation}} = \sqrt{\epsilon_m / \epsilon_0 c^2} \cdot P_{\text{excinction}}$. Note that this radiation pressure can be dominated by either scattering or absorption depending on the size and material properties of the particle; however, for subwavelength dielectric

particles, where the polarizability and cross-sections are small, is typically very weak.

Continuing with the Rayleigh approximation we can investigate how the induced dipole interacts with the external intensity distribution of light – i.e. the gradient force. This force, which pulls the particle into regions of higher electric field intensity, is ultimately the result of Lorentz forces^{55,56}:

$$F = (p \cdot \nabla)E + \frac{dp}{dt} \times B \quad \text{with} \quad p = \alpha E$$

$$F = \alpha \left((E \cdot \nabla)E + \frac{\partial E}{\partial t} \times B \right)$$

Using the vector identity $\nabla(A \cdot B) = A \times (\nabla \times B) + B \times (\nabla \times A) + (A \cdot \nabla)B + (B \cdot \nabla)A$ with $A = B = E$ yields:

$$\frac{1}{2} \nabla E^2 = E \times (\nabla \times E) + (E \cdot \nabla)E$$

Combining this vector identity with Faraday's law ($\nabla \times E = -\partial_t B$) allows us to rewrite the Lorentz force as:

$$F = \frac{1}{2} \alpha \nabla |E|^2 + \alpha \frac{\partial}{\partial t} (E \times B)$$

Taking the time average of this expression (i.e. averaging over the electromagnetic field oscillations) gives

$$F_{\text{gradient}} = \langle F \rangle_t = \frac{1}{4} \alpha \nabla |E|^2 + \alpha \mu_0 \frac{\partial I_0}{\partial t}$$

where μ_0 is the permeability of free space. For the case of a time-constant electric field intensity distribution this reduces to:

$$F_{\text{gradient}} = \frac{1}{4} \alpha \nabla |E|^2$$

As can be seen from the above, for a positive polarizability the gradient force always acts along the electric field intensity gradient, i.e. towards regions of higher electric field intensity. In the case of an optical trap, this means pulling particles in towards the focus of the laser beam. Note that from the form of the polarizability, for a dielectric particle to be trapped by this force it must have a higher relative permittivity than the surrounding medium. For lossless dielectric particle ($\sigma_{\text{absorption}} \sim 0$), the radiation pressure is dominated by scattering which is proportional to the volume of the particle squared;

therefore for smaller particles the gradient force (which is linearly proportional to the volume) tends to be dominant.

A Note on the Effect of Brownian Motion. From the above analysis it would appear that small lossless dielectric particles are *always* easier to optically trap than larger ones since the gradient force becomes more dominant as the particle size decreases. However, this is not the case. The Brownian motion of a particle is governed by the diffusion coefficient which is proportional to the thermal energy and inversely proportional to the drag acting on the particle. From Stokes' law for the drag force on spherical objects we know that the drag is proportional to the particle radius. Therefore, smaller particles experience significantly greater Brownian motion and therefore they tend to be less stably trapped than larger particles. This fact often prohibits optical trapping of dielectric nanoparticles. As a result, researchers have had to develop other means by which to amplify the optical gradient force to trap deeply subwavelength dielectric nanoparticles.

3.1.1 Plasmonic Optical Trapping

To overcome Brownian motion and stably trap dielectric nanoparticles the gradient force needs to be greatly enhanced. This can be achieved by confining light to a smaller area thereby increasing the electric field intensity gradient. However, there exists a fundamental limit to how tightly a lens can be used to focus light – “Abbe's diffraction limit”. To confine light beyond this limit, researchers have turned to plasmonics and specifically localized surface plasmon resonances (see section 2.1.4). Utilizing the enhanced electromagnetic field confinement provided by localized plasmonic resonances, research can amplify the optical gradient force to the point where dielectric nanoparticles can be stably trapped⁵⁷⁻⁶².

3.2 Plasmonic Anti-Stokes Thermometry

When illuminated by a laser a plasmonic particle will emit a broad inelastic radiation spectrum.⁶³⁻⁶⁵ This emission spectrum – often known as the surface enhanced Raman scattering (SERS) background – has been explained by several different mechanisms. Some proposed mechanisms by which this emission arises are: fluorescence via hot carrier recombination following plasmon decay^{66,67}, surface-enhanced fluorescence from contaminant molecules⁶⁸, Raman scattering from electrons within the metal⁶⁹⁻⁷¹, and damped image charges from nearby molecules⁷². While all these factors may contribute under certain circumstances, several works have tried to further elucidate this phenomenon. Inelastic emission has been observed on clean gold samples indicating that contaminant molecules cannot be the sole contribution to this effect.^{63,73} It has also been shown that the emission is present even if the excitation energy is below the onset of interband transitions indicating that d-s transitions are not necessarily required.⁷⁴ In 2001, Portales et al. have shown that for silver nano-crystals the emission

spectral peak is linearly related to the inverse of the cluster radius, and that similar spectra could be obtained with different excitation wavelengths – in agreement with a theory based on Raman scattering by single or collective electron-hole excitations.⁷¹ This theory of the emission spectra resulting from an inelastic electron scattering process is further supported by measurements on a gold SERS substrate reported by Hugall and Baumberg in 2015.⁶⁹ In this work the authors measure the inelastic emission from a SERS substrate and argue that the electric field confinement of the substrate can relax the momentum conservation condition enough to permit a Raman-like transition but not an s-s intraband transition. Conversely, in 2019 Cai et al. claimed that the emission is due to radiative recombination of hot carriers (either inter- or intra-band transitions) based on the power dependence of the emission intensities.⁷⁵

While the exact origin of this spectra is still under debate, it have been well shown experientially that the anti-Stokes side of this emission shows a strong temperature dependence and can be used as a far-field optical thermometer for plasmonic structures.^{62,69,76,77} The measured anti-Stokes inelastic emission, I_{AS} , has been observed to be described by the following equation:

$$I_{AS}(f, f_{Ex}, T) \propto n(f, f_{Ex}, T)S(f, f_{Ex})$$

here f is the frequency of the emission, f_{Ex} is the excitation (laser) frequency, and T is the temperature of the plasmonic particle. The term $n(f, f_{Ex}, T)$ is a Bose-Einstein thermal population factor, i.e.

$$n(f, f_{Ex}, T) = \left[\exp\left(\frac{h(f - f_{Ex})}{k_B T}\right) - 1 \right]^{-1}$$

where h, k_B are Plank's constant and Boltzmann's constant respectively. The factor $S(\nu, \nu_{Ex})$ is a frequency dependent optical scaling factor that accounts for both how effectively the plasmonic particle can scatter light into the far-field (as a function of wavelength) as well as the spectral response of the detector.

Thermometry Procedure. In the first demonstration of plasmonic inelastic emission as a thermometer, the plasmonic structures used had a relatively flat optical response such that $S \approx 1$. In that case, the anti-Stokes emission could be directly fit with a Boltzmann function at larger energy shifts to extract a temperature.⁶⁹ In order to utilize the anti-Stokes inelastic emission as a thermometer for plasmonic particles with a non-negligible spectral response (i.e. resonant nanoantennas, $S \neq 1$), a methodology similar to that proposed by Xu et al. can be used.⁷⁶ In this case, in order to remove the S term one reference spectra at a known temperature must be obtained. Utilizing this reference spectra and the spectra of a particle at an unknown temperature, the

ratio of the two spectra can be used to determine the unknown temperature according to:

$$\text{Ratio} = \frac{I_{AS}}{I_{AS}^{\text{ref}}} = \frac{n(\nu, \nu_{\text{Ex}}, T)}{n^{\text{ref}}(\nu, \nu_{\text{Ex}}, T^{\text{ref}})} = \frac{\exp\left(\frac{h(\nu - \nu_{\text{Ex}})}{k_B T^{\text{ref}}}\right) - 1}{\exp\left(\frac{h(\nu - \nu_{\text{Ex}})}{k_B T}\right) - 1}$$

A demonstration of this general thermometry procedure is shown below in Figure 15 where a temperature-controlled stage is used to validate the results. A plasmonic particle (or collection of particles) is illuminated with a monochromatic laser and the inelastic emission is recorded (Figure 15a). As the temperature of the stage is increased it can be readily observed that an increasing proportion of the anti-Stokes signal comes from higher energy shifts as expected due to the Bose-Einstein thermal population factor (Figure 15b). These anti-Stokes spectra are then divided by the reference spectra and fit with the ratio of two Bose-Einstein thermal population factors above to obtain the extracted temperature (Figure 15c). As shown in Figure 15d, this thermometry procedure can accurately determine the temperature of a plasmonic particle over a wide range of temperatures.

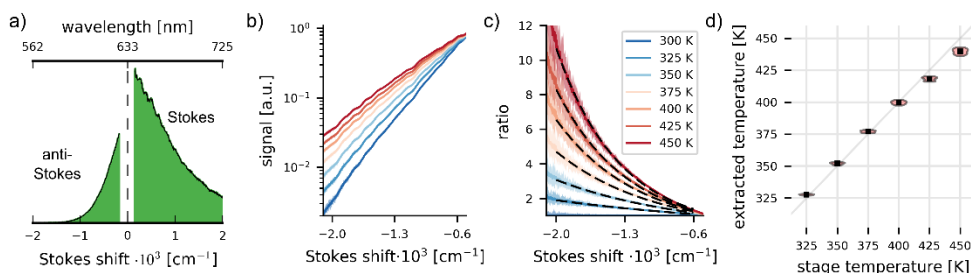


Figure 15 Procedure for anti-Stokes thermometry. a) Photoluminescence emission spectrum from a single gold nanoantenna. Excitation wavelength = 633 nm. b) Anti-Stokes emission intensity at different temperatures. Signal is normalized to the emission intensity at -500 cm⁻¹. c) Ratio of each spectrum in image b to the reference spectrum obtained at 300 K (dark blue). Dashed lines are the numerical fit based on the ratio of two Bose-Einstein thermal population factors. d) Extracted temperatures from numerical fits plotted against the known stage temperature. Extracted temperatures are based on the relative changes in anti-Stokes emission intensity as a function of energy shift. Reprinted with permission from⁶². Copyright 2018 American Chemical Society.

3.3 Observing Thermophoresis via Fluorescence Microscopy

To study the thermophoretic depletion due to localized heating of a plasmonic structure epifluorescence microscopy was used. This technique, illustrated in Figure 16, utilizes the projected (imaged) fluorescence intensity profile to extract the local concentration of fluorescent particles. To determine the local concentration from the projected image a model-based deconvolution algorithm is used.

In the example presented here, a 1064 nm laser is focused onto a plasmonic antenna to induce heating. The sample cell is filled with a dilute solution of

Experimental Methods

100 nm diameter fluorescent polystyrene spheres. The sample is uniformly illuminated at the fluorescence excitation wavelength. Filters are used to remove the 1064 nm laser and the fluorescence excitation wavelength from the imaging path and the fluorescence emission profile is imaged with a camera. In practice, if the fluorescence excitation illumination is not perfectly uniform then it is necessary to obtain a reference image of the system with no heating laser and divide all subsequent images by this reference image to highlight changes in the intensity profile.

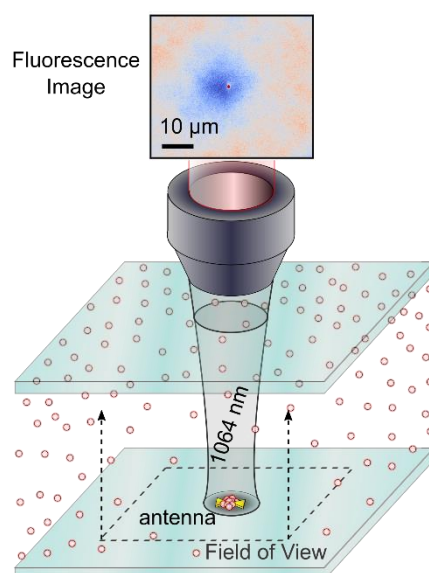


Figure 16 Observing thermophoresis with epifluorescence microscopy. Schematic overview of the experimental setup used to observe thermophoresis. A plasmonic antenna (yellow, centre of field of view) is illuminated with a 1064 nm laser which causes heating. Some fluorescent particles (red circles) are optically trapped by the plasmonic structure, while others are thermophoretically repelled. The field of view is uniformly illuminated at the fluorescence excitation wavelength and an image is recorded. Far from the antenna, the relative fluorescence intensity is indicative of the local concentration of fluorescent particles (high intensity = red, low intensity = blue). Reprinted with permission from⁶². Copyright 2018 American Chemical Society.

After recording the fluorescence intensity profile, the radial average (centred at the heating antenna) is calculated as shown in Figure 17. This radial averaging reduces the amount of noise that is contributed from local stochastic fluctuation in particle density, as well as reducing the influence of instances of particle aggregation.

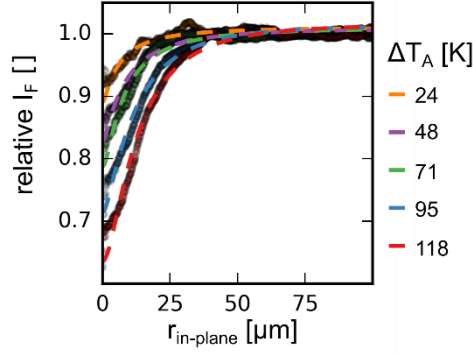


Figure 17 Radially averaged fluorescence intensity profiles. The fluorescence intensity is radially averaged centred around the plasmonic antenna. This is recorded for different heating laser powers which correspond to different antenna temperatures. Reprinted with permission from⁶². Copyright 2018 American Chemical Society.

The radially averaged intensity profile results from a 2D projection of the 3D concentration profile. To account for out-of-plane fluorophores, the spatial light collection efficient function (CEF) of the imaging objective must be determined. The CEF of microscope objectives has previously been studied for applications in particle flow cytometry.^{78,79} These results indicate good agreement between experimental results and CEFs calculated by other means such as geometric optics, wave optics, or Monte-Carlo ray-tracing simulations. A modified CEF based on the geometric optics “blur-circle” method is used here for its simplicity and numerical expediency. In this approximation to the CEF an isotropic point source (i.e. fluorescent nanoparticle) that is displaced from the image plane will project itself as a uniform intensity circle onto the image plane. The size of the projected circle depends on the distance from the image plane as well as the numerical aperture of the microscope objective. This method therefore accounts for the loss in spatial resolution but significant integrated signal that is imaged due to background fluorophores.

The collection efficiency of a rectangular aperture in the image plane (e.g. detector pixel) due to a microscope objective with numerical aperture $NA = n_m \sin \psi$, the CEF is given by:⁷⁹

$$\text{CEF}(x, y, z) = \frac{1}{1\pi(1 - \cos \psi)} \int_{v_{\min}}^{v_{\max}} dv \frac{|x|}{x^2 + (v - y)^2} \times \left[\frac{w - z}{(x^2 + (v - y)^2 + (w - z)^2)^{1/2}} \right]_{w_{\min}(v)}^{w_{\max}(v)}$$

with

$$w_{\min}(v) = \max \left[-\frac{h}{2}, \quad z - (x^2 \tan^2 \psi - (v - y)^2)^{1/2} \right],$$

$$w_{\max}(v) = \min \left[\frac{h}{2}, \quad z + (x^2 \tan^2 \psi - (v - y)^2)^{\frac{1}{2}} \right],$$

and

$$v_{\min} = \max \left[-\frac{d}{2}, \quad y - |x| \tan \psi \right],$$

$$v_{\max} = \min \left[\frac{d}{2}, \quad y + |x| \tan \psi \right],$$

Here, the rectangular aperture has width d and height h . This equation calculates the overlap between the projected “blur-circle” and the rectangular slit while only accepting angles which are captured by the NA of the objective. In the case of a lossless medium, this equation implies that all planes parallel to the focal plane, but offset along z , contribute equally to the total integrated intensity at the rectangular aperture. This method assumes that the numerical aperture of the objective does not change appreciably for planes displaced from the focal plane; this has been experimentally confirmed for distances on the order of 100 μm from the focal plane.⁷⁸

To utilize the CEF to reconstruct the *real* thermophoretic depletion from the observed projected intensity, an iterative least squares fitting algorithm is used (summarized in Figure 18). This procedure assumes that an orbitally symmetric depletion profile exists which is described by $c/c_0 = \exp(-S_T \Delta T)$. The Soret coefficient is also assumed to have the following temperature dependence as has been previously observed experimentally:⁸⁰

$$S_T(T) = S_T^\infty \left[1 - \exp\left(\frac{T^* - T}{T_0}\right) \right]$$

here, S_T^∞ is the high temperature limit, T^* is the temperature at which the behaviour changes from thermophilic to thermophobic, and T_0 determines how strongly the Soret coefficient depends on temperature.

For every observed point in the radially averaged intensity profile, a cone of acceptance defined by the numerical aperture is projected through the medium, and the fluorescence intensity observed from this cone is calculated based on the CEF and the assumed concentration profile. This process is then repeated and the Soret coefficient constants are updated until the projected intensity profile matches the experimental results. In addition, the temperature dependence of the fluorescence emission is also accounted for in this procedure.

Experimental Methods

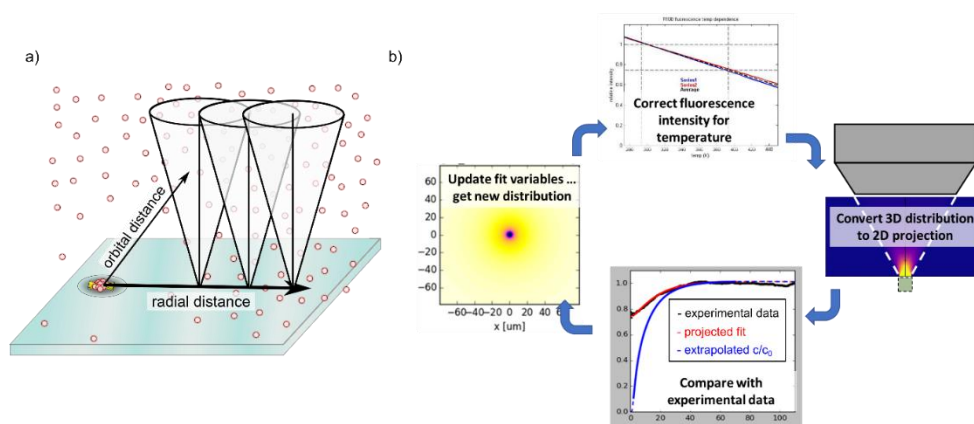


Figure 18 Method of extracting the true thermophoretic depletion via a model-based deconvolution scheme. a) Schematic overview of the procedure. The observed intensity profile is a contribution from all planes of the system containing fluorescent particles based on the collection efficient function of the microscope objective (indicated by the cones). b) Procedure for extracting the true thermophoretic depletion. A 3D concentration profile is assumed for a reasonable value of the Soret coefficient and the depletion is calculated based on the temperature profile. The temperature dependent fluorescence intensity at each point is corrected for. The light collection efficient function is used to determine the corresponding 2D projection of this concentration profile. The 2D projection is then compared with the experimental data. The fitting parameters used are iteratively updated until the calculated projection closely matches the experimental data and the corresponding 3D concentration profile is used for the extracted thermophoretic depletion. Reprinted with permission from⁶². Copyright 2018 American Chemical Society.

After the model-based deconvolution is completed an estimate for the true concentration profile is obtained as shown in Figure 19. It is interesting to note, that while the observed intensity variation was at most less than 40%, this corresponds to a local depletion of almost 100% immediately adjacent to the heated plasmonic structure. To mitigate the effect of out-of-plane fluorescent particles and ensure a good signal to noise ratio of the detected depletion it is helpful to use thin sample chambers thereby reducing the amount of background fluorescence.

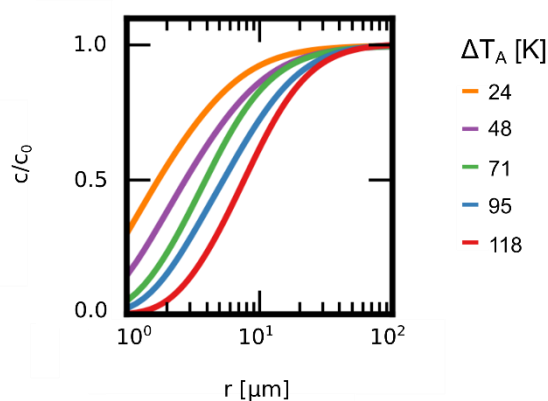


Figure 19 Extracted thermophoretic depletion profiles. Data shown above is the extracted thermophoretic depletion profiles for different antenna temperatures. Results are based on the experimental data shown in Figure 17 and the procedure shown in Figure 18. Reprinted with permission from⁶². Copyright 2018 American Chemical Society.

3.4 Observing Plasmonic Nano-Bubbles via Optical Backscattering

When making thermoplasmonic nanobubbles it is necessary to measure the presence of such nanobubbles; however, directly imaging such small bubbles is difficult for two fundamental reasons. First, small bubbles can be difficult to accurately image with optical microscopy, particularly when the nanobubbles approach the resolution limit of an imaging system – i.e. only a few hundred nanometres in diameter or less. Additionally, the presence of other optical effects – such as autofluorescence – can obfuscate the image. The second fundamental issue with measuring such small bubbles is that their lifetime is expected to be significantly shorter than larger microbubbles and therefore the limited time resolution of most cameras is not adequate. This second issue is further compounded since small bubbles can require significant integration times to overcome shot noise.

To bypass these issues, an alternative measurement technique is desirable when measuring small thermoplasmonic nanobubbles with short lifetimes. One such technique involves utilizing the backscattering of a constant power detection laser. This method of backscattering bubble detection was pioneered by the Orrit group in 2015 for detecting explosive thermoplasmonic bubbles in pentane.³¹ As previously mentioned in section 2.4, the results obtained for thermoplasmonic bubbles formed in other solvents (and especially n-alkanes) cannot be readily extended to the results obtained for thermoplasmonic bubbles formed in water.^{5,30} Regardless, the backscattering experimental approach can be utilized to study thermoplasmonic nanobubbles in water.

Measurement Details. The experimental setup used to generate and detect thermoplasmonic nanobubbles is shown in Figure 20a. A 532 nm continuous wave heating laser is focused through a microscope objective onto the sample and aligned with the plasmonic heating structures. The intensity of the 532 nm heating laser is controlled with an acousto-optic modulator. A second laser at constant power is used to detect the presence of a bubble via changes in the backscattering intensity. In the experiments performed here, this detection laser had a wavelength of 1064 nm.

To ensure that only small nanobubbles were created, different isolated gold nanostructures were used as the plasmonic heating elements (Figure 20b). This was done to ensure that the temperature increase did not extend far into the water medium, thereby limiting the extent to which a thermally formed bubble can grow. This is in contrast with past works that used continuous plasmonic arrays or films to generate heat from laser that had been focused down to a diameter of several microns. In the latter case, the temperature increase from plasmonic heating structure extends far away from the interface into the water due to the large heat source density. The plasmonic structures

Experimental Methods

used for heating in this study are collections of several gold disks with a nominal height of 60 nm and diameter of 100nm, the interparticle spacing (edge to edge) is designed to be 50 nm. As shown in the darkfield scattering spectra in Figure 20b, by using collections of uniform plasmonic disks all structures resonate at approximately the same wavelength (≈ 650 nm); this ensures that all structures interact strongly with the heating laser, while being significantly detuned from the detection laser.

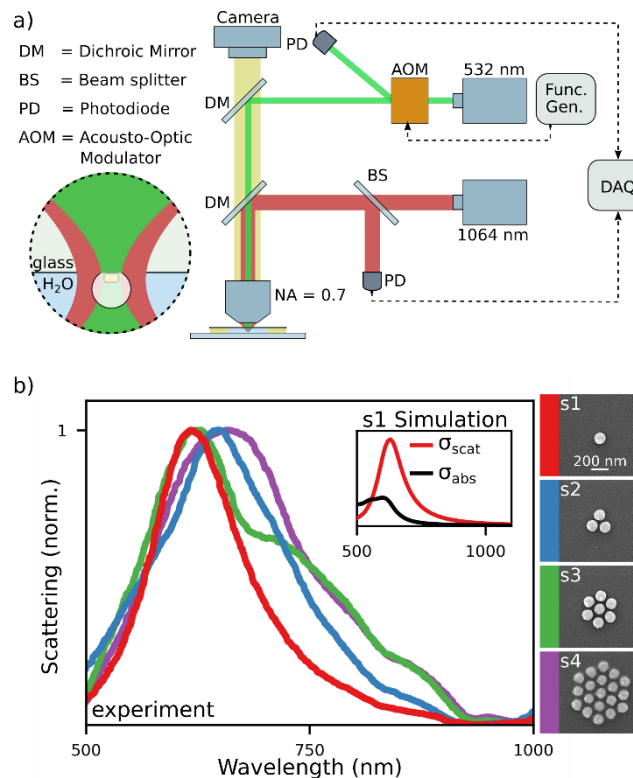


Figure 20 Experimental setup and structures used for generation and detection of thermoplasmonic nano-bubbles. a) Schematic overview of the experimental setup. A 532 nm laser is used for heating the plasmonic structures, the intensity of the heating laser is controlled with an acousto-optic modulator (AOM). A constant power 1064 nm laser is co-aligned with the heating laser and the back-scattering signal is detected to infer the presence of a bubbles. Both the backscattering signal and the heating laser power are monitored with a digital acquisition device (DAQ). b) Different arrangements of plasmonic particles are used for bubble generation (right – SEM images). These structure all show similar darkfield scattering profiles. Inset shows the simulated absorption and scattering cross sections for structure s1.

Provided here is a generalized overview of the procedure for bubble formation and detection. The main goal is to simultaneously probe both the heating laser power and the backscattering intensity. As the 532 nm heating laser is modulated by an acousto-optic modulator, the 1st order diffracted light is aligned into the microscope and focused onto the plasmonic nanostructures; meanwhile the 0th order diffracted light is detected by a photodiode. As the 1st order light and 0th order light are linearly related to one another a calibration can be made to convert the 0th order light measured in volts by the photodiode to the power of the 1st order light which reaches the sample.

Once this calibration has been performed the heating laser power and the backscattered intensity can then be simultaneously monitored by a data

acquisition device. The detection laser is maintained at constant power so changes in the backscattering signal therefore originate from changes to the optical properties of the system immediately surrounding the plasmonic structures and can be used to detect the presence of a bubbles. Since the data acquisition device performed multiplexed sampling the two measurements do not occur at exactly the same time – i.e. each channel is measured in series with a slight delay between channels. This discrepancy must be accounted for and a correction to the time stamp of one channel versus the other included in the data analysis, this issue is particularly impactful when using high acquisition rates to observe fast processes.

Finally, the experiment can be performed. When the heating laser reaches the threshold power required for bubble formation, a nearly instantaneous change in the backscattered signal is observed due to the formation of a bubble (see Figure 21). Prior to bubble formation some modulation of the backscattered signal is observed due to the temperature dependence of the optical properties of the system – specifically temperature dependence refractive index changes in the water and glass cause changes in reflection from the glass/water interface. Nevertheless, the significant change in the backscattering due to bubble formation clearly dominates these thermally induced changes as the change in effective refractive index of the medium due to the presence of a bubble is drastic when compared to temperature induced refractive index changes in water.

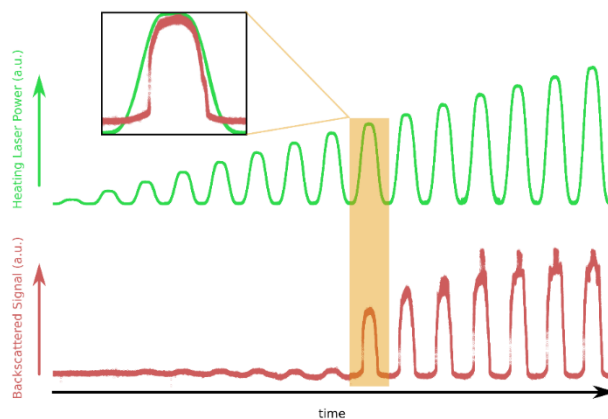


Figure 21 Detecting bubbles. The top row (green) shows real time measurements of the heating laser power. In this case the heating laser is modulated by the acousto-optic modulator with a sine wave profile. The bottom row (red), shows the corresponding backscattered signal from the detection laser. Once the heating laser has reached a certain threshold for bubble formation, a discrete change in the backscattered signal is observed which occurs due to the change in optical properties of the system due to the formation of a bubble. The inset shows one cycle series which corresponds to the initial bubble formation. Each “cycle” in the data presented above is the data from several successive measurement super imposed on one another.

Interpreting the Signal. While it is tempting to assume that the backscattering signal is linearly (or at least monotonically) correlated to changes in the bubble radius, this is not necessarily the case. To investigate how changes in bubble size affects the backscattering signal finite difference time domain simulations were performed. In these simulations the plasmonic

Experimental Methods

antenna used was a single gold disk modelled to accurately reflect the geometry of the structure based on scanning electron microscope images. The permittivity of the antenna was based on the Johnson and Christy dielectric function for gold. The substrate and superstrate (water) were given constant refractive indices of 1.5 and 1.33 respectively. An incident Gaussian beam with a wavelength of 1064 nm and a minimum beam waist radius of 800 nm was used to illuminate the structures from the side of the substrate. The backscattered signal was collected over a large area and was propagated into the farfield to account for the numerical aperture of the collection objective ($NA = 0.7$). The bubble was modelled as an air-filled sphere with a variable radius for different predefined contact angles – 30, 60, 90, and 120 degrees as measured between the bubble surface and the substrate interface.

The results, shown below in Figure 22, indicate that while the backscattering signal nominally increases with increasing bubble diameter, large Fabry-Perot like resonances were observed. The periodicity of these oscillations depends on the contact angle with a periodicity defined by the total height of the bubble above the substrate. The amplitude of the oscillations decreased slightly with increasing numerical aperture, however they are always present. From this result it can be concluded that the backscattering intensity alone cannot be used to determine the bubble size; however, the fact that the signal is appreciably increased for a bubble with any radius implies that it is possible to use this signal to detect the presence of a bubble – i.e. as a binary measure of if a bubble is or is-not present.

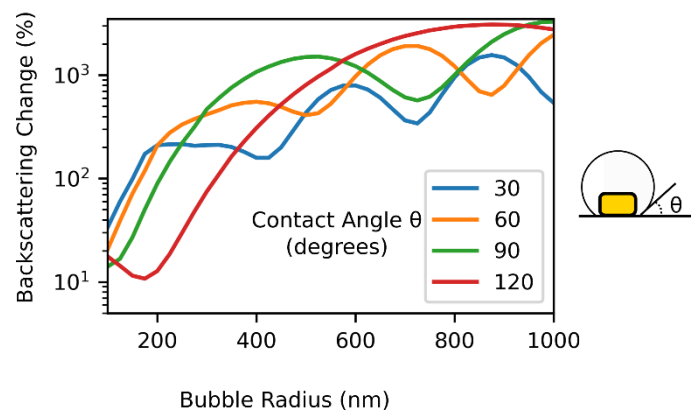


Figure 22 Effect of bubble radius and contact angle on changes in the backscattered intensity. As the bubble expands oscillations in the backscattered signal are observed. The periodicity of these oscillations depends primarily on the bubble height.

4 Summary of Appended Papers

The research that comprises this thesis essentially follows the questions that was outlined in the introductions: what happens when you shoot a laser at a piece of gold in a microfluidic environment and turn the power up? The basic experimental setup consists of a gold nanostructure on a glass substrate immersed in water that is excited by a focused laser beam. In paper I the thermal effects on colloidal particles are explored for moderate temperature increases; specifically the interplay between optical forces and thermal effects nearby the antenna and the thermophoretic depletion of analytes at farther distances. In paper II we explore what happens when the laser power is increased further and the onset of bubble formation.

4.1 Paper I: Photothermal Heating of Plasmonic Nanoantennas: Influence on Trapped Particle Dynamics and Colloid Distribution

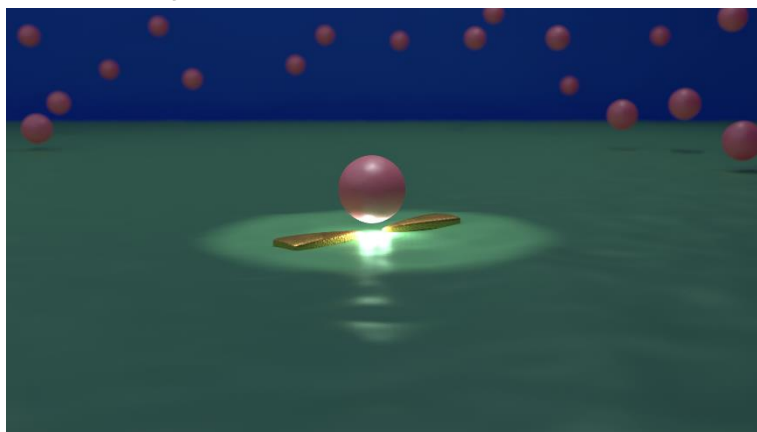


Figure 23 Table of contents figure from paper I. Here we see a plasmonic antenna that is optically excited producing a localized electric field enhancement. The local field enhancement can optically trap dielectric nanoparticles; however, the heat generated tends to push particle away thereby reducing the probability for trapping.

This study was motivated by the field of plasmonic optical trapping (section 3.1.1). In plasmonic optical trapping the electric field confinement provided by plasmonic nanostructures is used to enhance the optical gradient force thereby allowing smaller particle to be trapped than is possible with a conventional optical trapping setup (i.e. one which uses only farfield optics). This method can be combined with other spectroscopic techniques, such as surface enhanced Raman spectroscopy, to enable identification of the trapped particle or the investigation of other properties. While the ability of plasmonic optical traps to impart forces and localize small dielectric nanoparticles has been demonstrated on many occasions, often the associated thermal effects have been ignored. The absence of specific studies which investigate the interplay between optical forces and thermal effects is noteworthy since there also exists studies which directly use thermal forces to manipulate particles in an experimental configuration remarkably similar to those used in plasmonic optical traps.

In this work, I developed a standard plasmonic optical trapping platform utilizing gold bowtie nanoantennas as an optical transducer to impart forces on colloidal dielectric nanoparticles. Facilitated by recent advances in thermometry of plasmonic structures (see section 3.2) I was able to directly measure the temperature of the plasmonic structures while being optically excited for the purposes of plasmonic trapping. Utilizing these temperature measurements, I could compare the how the effective trapping potential varied for plasmonic antenna with different resonance conditions.

As expected, if the resonance wavelength of the plasmonic antenna was close to the excitation wavelength then enhanced confinement was observed at lower excitation powers. This simply results from the fact that there is greater interaction between the antenna and the excitation laser resulting in more efficient electric field enhancement and therefore greater optical forces. However, structures that are resonant with the excitation laser are also heated more efficiently. When the trapping characteristics of the same antennas were compared with each other in terms of temperature rather than incident power there was a surprising invariance in the trapping capabilities. Essentially, the degree of particle confinement for all structures was nearly identical for the same local temperature. This result implies that although a resonant structure can reduce the input power required to plasmonically trap a particle, because heat is also generated more efficiently there is no benefit to using resonant structures for trapping temperature sensitive analytes.

Of even greater importance is the effect that this plasmonic heating on nearby particles that have not been optically trapped. As discussed in section 2.3, the presence of a temperature gradient induces particle to move thermophoretically, typically towards colder regions – i.e. away from the antenna. This is significant since plasmonic optical traps are not mobile, the standard method used to trap a particle is to optically excite the antenna and wait for the analyte to randomly diffuse towards the particle where it will then be held by optical forces. However, since the induced temperature gradient effectively repels particles from the antenna this can act to prohibit optical trapping or at least make it significantly less likely. Because the temperature profile extends for several microns away from the antenna (while optical forces are only significant for a few hundred nanometers at best) particles will typically only experience these thermophoretic effects. Using epifluorescence microscopy (section 3.3), I was able to directly observe the extent of thermophoretic depletion and compare this with the local temperature increase of the plasmonic antenna. I found that the depletion could extend for several microns away from the plasmonic antenna, meaning that while the optical forces can in principle trap a nearby particle the system is thermally influenced at much larger distances.

This result is very significant in terms of making an efficient plasmonic trapping platform, but also has implications in other fields. For instance, many

works have used plasmonic structures for passive sensing as opposed to for manipulation. One such scheme is to functionalize the gold surface and monitor the resonance condition via darkfield scattering. As analytes bind to the functionalized surface they modify the local refractive index and therefore the resonance condition. This is the basis of localized surface plasmon resonance sensors. While the intensity of white light used in these schemes is often much less than the laser intensity used in trapping, there can still potentially be a local temperature increase of a few Kelvin at least. Because of the exponential dependence of local concentration on temperature this can induce non-negligible effects the observed signal response which affects the extracted binding parameters. In this regard, paper I serves as a guideline for how thermophoretic depletion can affect any system that utilizes plasmonic particles as a means of manipulating or sensing analytes in solution and why these thermophoretic effects are so important to consider.

4.2 Paper II: Ultrafast Modulation of Thermoplasmonic Nano-Bubbles in Water

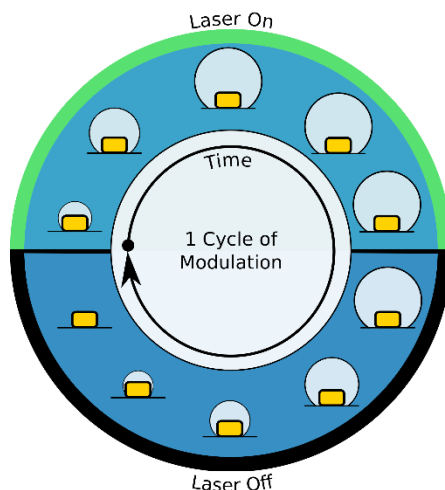


Figure 24 The lifecycle of a bubble. Shown here is the proposed lifecycle of a bubble forced around a plasmonic particle due to thermoplasmonic heating. While this process has been studied significantly for larger microbubbles, the details of this process had thus far been unknown for plasmonic nanobubbles in water.

Recently there has been significant interest in the formation of bubbles around plasmonic structures which are excited by a continuous wave laser. The formation of a bubble can induce many interesting effects such as Marangoni flows (see section 2.4). Typically, in microfluidic systems, fluid flow is governed by laminar flow, and as a result mixing two different streams can be difficult – one possible use of plasmonic bubbles is to create turbulent Marangoni flows that facilitate mixing. Recent studies on bubble formation/dissipation and the associated Marangoni flows have typically focused on large microbubbles that tend to be relatively stable. This stability means that even after laser illumination has stopped the bubble will persist for a significant amount of time (tens to hundreds of seconds). This is a problem for many high throughput applications since the long dissipation

time effectively limits the rate at which the system can be addressed. One method to improve the effective throughput is by creating smaller nanobubbles.

There are two difficulties with creating smaller nanobubbles. First, in many experimental configurations it is difficult to prevent a thermoplasmonic bubble from growing into a microbubble. Second, it is difficult to observe nanobubble formation/dissipation which therefore creates a barrier to optimizing systems in this regard. In paper II we utilized optical backscattering to directly observe nanobubble formation (see section 3.4) and study how the bubble formation is affected by the plasmonic structure size. Our findings showed that the size of the plasmonic structure determines how small of a bubble can be made (i.e. how fast the bubble can dissipate). This results from the efficiency that a plasmonic structure can heat its environment. Essentially, the smaller a structure is the more localized the heating and therefore the smaller the bubble is and the faster it dissipates. I was able to directly measure the decay time of these bubbles and found that it could vary from several tens of microseconds for a plasmonic structure with a diameter of 100 nm, to 10 milliseconds for a plasmonic structure with an overall diameter of 700 nm. This decay time is the limiting factor for determining the maximum possible modulation frequency of the bubble, and therefore the maximum throughput in addressing the system. I observed nanobubble modulation up to a few kilohertz for small structures, while larger structures could only be modulated up to 100 Hz.

5 Conclusion & Outlook

Contained within this thesis are two studies that investigate what happens when you shoot a laser at a piece of gold in water and turn the power up. As seems to be a theme within thermoplasmonics there are both beneficial and detrimental effects. For instance, the heat generated when gold nanostructures are illuminated tends to cause some degree of thermophoretic depletion of surrounding analytes. In many cases this may be disadvantageous and care must be taken to mitigate this effect; and yet, plenty of studies exist that demonstrate how instead this thermophobic response can directly be used for particle manipulation or to sense small molecule binding. If you turn the power up bubble formation occurs. The formation of a bubble can cause a significant increase in the temperature of the gold particle which can result in irreversible damage to the structure. However, if this temperature increase is mitigated, the presence of a bubble has shown to be an advantageous way to impart extremely large forces on the nano-/micro-scale using farfield illumination.

For the continuation of these studies, one area that seems promising is to investigate how Marangoni flows are affected by making smaller nanobubbles, and if modulation of the bubble has any observable effect on these Marangoni flows. Theoretically it has been suggested that smaller bubbles should induce larger flow rates. This has been experimentally observed to a limited extent for microbubbles and it would be interesting to see if this trend extends to the nanoscale. Additionally, the time dynamics should prove interesting. Bubble formation seems to be incredibly rapid and a significant shockwave might be produced as a result. It is also unclear how the rate of change of the bubble diameter affects Marangoni flows.

Another study that could be useful to the community is to perform a localized surface plasmon resonance sensing experiment at different white light intensities to see how titration-style binding experiments are affected by thermophoresis. For higher light intensities there is obviously a greater signal to noise ratio; however, this also induces localized heating which leads to thermophoretic effects. In this case the *true* local concentration of analytes might be different from the bulk value resulting in a shift in the binding curves which could give erroneous binding constants. The extent of this effect could be significantly impactful when studying binding kinetics at the single molecule level.

References

1. Hecht, E. *Optics*. (Addison Wesley, 2002).
2. Li, Y. *Plasmonic Optics: Theory and Applications*. (SPIE Press, 2017).
3. Kerker, M. *The Scattering of Light and Other Electromagnetic Radiation. Chap 7*, (1969).
4. Maier, S. A. *Plasmonics: Fundamentals and applications. Plasmonics: Fundamentals and Applications* (2007). doi:10.1007/0-387-37825-1
5. Baffou, G. *Thermoplasmonics*. (University Printing House, 2018). doi:10.1017/9781108289801
6. Donner, J. S., Baffou, G., McCloskey, D. & Quidant, R. Plasmon-assisted optofluidics. *ACS Nano* **5**, 5457–5462 (2011).
7. Cengel, Y. A. *Heat transfer: a practical approach*. (McGraw-Hill, 2003).
8. Baffou, G., Quidant, R. & Girard, C. Thermoplasmonics modeling: A green's function approach. *Phys. Rev. B - Condens. Matter Mater. Phys.* **82**, 1–11 (2010).
9. Berto, P., Mohamed, M., Rigneault, H. & Baffou, G. Time-harmonic optical heating of plasmonic nanoparticles. *Phys. Rev. B* **90**, 035439 (2014).
10. Piazza, R. Thermophoresis: moving particles with thermal gradients. *Soft Matter* **4**, 1740 (2008).
11. Putnam, S. A. & Cahill, D. G. Transport of nanoscale latex spheres in a temperature gradient. *Langmuir* **21**, 5317–5323 (2005).
12. Duhr, S. & Braun, D. Thermophoretic depletion follows boltzmann distribution. *Phys. Rev. Lett.* **96**, 8301 (2006).
13. Würger, A. Hydrodynamic Boundary Effects on Thermophoresis of Confined Colloids. *Phys. Rev. Lett.* **116**, 1–5 (2016).
14. Putnam, S. A., Cahill, D. G. & Wong, G. C. L. Temperature dependence of thermodiffusion in aqueous suspensions of charged nanoparticles. *Langmuir* **23**, 9221–9228 (2007).
15. Braibanti, M., Vigolo, D. & Piazza, R. Does thermophoretic mobility depend on particle size? *Phys. Rev. Lett.* **100**, 8303 (2008).
16. Würger, A. Thermal non-equilibrium transport in colloids. *Reports Prog. Phys.* **73**, 6601 (2010).
17. Iacopini, S., Rusconi, R. & Piazza, R. The ‘macromolecular tourist’:

References

- Universal temperature dependence of thermal diffusion in aqueous colloidal suspensions. *Eur. Phys. J. E* **19**, 59–67 (2006).
18. Lin, L. *et al.* Opto-thermoelectric nanotweezers. *Nat. Photonics* **12**, 195–201 (2018).
 19. Jerabek-Willemsen, M., Wienken, C. J., Braun, D., Baaske, P. & Duhr, S. Molecular Interaction Studies Using Microscale Thermophoresis. *Assay Drug Dev. Technol.* **9**, 342–353 (2011).
 20. Seidel, S. A. I. *et al.* Microscale thermophoresis quantifies biomolecular interactions under previously challenging conditions. *Methods* **59**, 301–315 (2013).
 21. Wienken, C. J., Baaske, P., Rothbauer, U., Braun, D. & Duhr, S. Protein-binding assays in biological liquids using microscale thermophoresis. *Nat. Commun.* **1**, 1–7 (2010).
 22. Braun, M. & Cichos, F. Optically controlled thermophoretic trapping of single nano-objects. *ACS Nano* **7**, 11200–11208 (2013).
 23. Braun, M., Bregulla, A. P., Günther, K., Mertig, M. & Cichos, F. Single Molecules Trapped by Dynamic Inhomogeneous Temperature Fields. *Nano Lett.* **15**, 5499–5505 (2015).
 24. Lin, L. *et al.* Interfacial-entropy-driven thermophoretic tweezers. *Lab Chip* **17**, 3061–3070 (2017).
 25. Kroy, K., Chakraborty, D. & Cichos, F. Hot microswimmers. *Eur. Phys. J. Spec. Top.* **225**, 2207–2225 (2016).
 26. Bregulla, A. P., Yang, H. & Cichos, F. Stochastic localization of microswimmers by photon nudging. *ACS Nano* **8**, 6542–6550 (2014).
 27. Baraban, L. *et al.* Fuel-free locomotion of janus motors: Magnetically induced thermophoresis. *ACS Nano* **7**, 1360–1367 (2013).
 28. Wang, Y. *et al.* Vapor and Gas-Bubble Growth Dynamics around Laser-Irradiated, Water-Immersed Plasmonic Nanoparticles. *ACS Nano* **11**, 2045–2051 (2017).
 29. Baffou, G., Polleux, J., Rigneault, H. & Monneret, S. Super-Heating and Micro-Bubble Generation around Plasmonic Nanoparticles under CW Illumination. *J. Phys. Chem. C* **118**, 4890–4898 (2014).
 30. Zaytsev, M. E. *et al.* Plasmonic Bubbles in n-Alkanes. *J. Phys. Chem. C* **122**, 28375–28381 (2018).
 31. Hou, L., Yorulmaz, M., Verhard, N. R. & Orrit, M. Explosive formation and dynamics of vapor nanobubbles around a continuously heated gold nanosphere. *New J. Phys.* **17**, (2015).

References

32. Wang, Y. *et al.* Giant and explosive plasmonic bubbles by delayed nucleation. *PNAS* **115**, 7676–7681 (2018).
33. Liu, X., Bao, L., Dipalo, M., De Angelis, F. & Zhang, X. Formation and dissolution of microbubbles on highly-ordered plasmonic nanopillar arrays. *Sci. Rep.* **5**, 1–9 (2015).
34. Mizerovsky, L. N. & Smirnova, K. P. Temperature dependence of the solubility of nitrogen in n-alkanes at atmospheric pressure. *Russ. Chem. Bull.* **59**, 673–676 (2010).
35. Deguchi, S., Takahashi, S., Hiraki, H. & Tanimura, S. Direct measurement of force exerted during single microbubble generation. *Appl. Phys. Lett.* **102**, 804101 (2013).
36. Namura, K., Nakajima, K. & Suzuki, M. Quasi-stokeslet induced by thermoplasmonic Marangoni effect around a water vapor microbubble. *Sci. Rep.* **7**, 1–8 (2017).
37. Ljunggren, S. & Eriksson, J. C. The lifetime of a colloid-sized gas bubble in water and the cause of the hydrophobic attraction. *Colloids Surfaces A* (1997).
38. Li, J. *et al.* Photothermal Generation of Programmable Microbubble Array on Nanoporous Gold Disks. *Opt. Express* **26**, 18964–18969 (2018).
39. Zhao, C., Liu, Y., Zhao, Y., Fang, N. & Huang, T. J. A reconfigurable plasmofluidic lens. *Nat. Commun.* **4**, 1–8 (2013).
40. Gan, F. *et al.* Widely Tuning Surface Plasmon Polaritons with Laser-Induced Bubbles. *Adv. Opt. Mater.* **5**, 1600545 (2017).
41. Zhang, K. *et al.* Laser-induced thermal bubbles for microfluidic applications. *Lab Chip* **11**, 1389–1395 (2011).
42. Kim, H., Bai, H., Zhang, Z., Kusimo, A. & Yu, M. Optofluidic microvalve-on-a-chip with a surface plasmon-enhanced fiber optic microheater. *Biomicrofluidics* **8**, 054126 (2014).
43. Namura, K., Nakajima, K., Kimura, K. & Suzuki, M. Photothermally controlled Marangoni flow around a micro bubble. *Appl. Phys. Lett.* **106**, 1–6 (2015).
44. Setoura, K., Ito, S. & Miyasaka, H. Stationary bubble formation and Marangoni convection induced by CW laser heating of a single gold nanoparticle. *Nanoscale* **9**, 719–730 (2017).
45. Namura, K., Nakajima, K., Kimura, K. & Suzuki, M. Sheathless particle focusing in a microfluidic chamber by using the thermoplasmonic Marangoni effect. *Appl. Phys. Lett.* **108**, 1–4 (2016).

References

46. Namura, K., Nakajima, K. & Suzuki, M. Investigation of transition from thermal- to solutal-Marangoni flow in dilute alcohol / water mixtures using nano-plasmonic heaters. *Nanotechnology* **29**, 1–7 (2018).
47. Takahashi, K., Weng, J. & Tien, C. Marangoni Effect in Microbubble Systems. *Microscale Thermophys. Eng.* **3**, 169–182 (1999).
48. Blake, J. R. & Chwang, A. T. Fundamental singularities of viscous flow. Part I: The image systems in the vicinity of a stationary no-slip boundary. *J. Eng. Math.* **8**, 23–29 (1974).
49. Zheng, Y. *et al.* Accumulating microparticles and direct-writing micropatterns using a continuous-wave laser-induced vapor bubble. *Lab Chip* **11**, 3816–3820 (2011).
50. Li, Y., Xu, L. & Li, B. Gold nanorod-induced localized surface plasmon for microparticle aggregation. *Appl. Phys. Lett.* **101**, (2012).
51. Ashkin, A. Acceleration and Trapping of Particles by Radiation Pressure. *Phys. Rev. Lett.* **24**, 156–159 (1970).
52. Ashkin, A., Dziedzic, J. M., Bjorkholm, J. E. & Chu, S. Observation of a single-beam gradient force optical trap for dielectric particles. *Opt. Lett.* **11**, 288–290 (1986).
53. Jones, P. H., Marago, O. M. & Volpe, G. *Optical Tweezers Principles and Applications*. (Cambridge University Press, 2015).
54. Stratton, J. A. *Electromagnetic Theory. Library* **14**, (1941).
55. Gordon, J. P. Radiation Forces and Momenta in Dielectric Media. *Phys. Rev. A* **8**, 14–21 (1973).
56. Griffiths, D. & College, R. *Introduction to electrodynamics. Zhurnal Eksperimental'noi i Teoreticheskoi Fiziki* (1999). doi:10.1007/978-1-4612-2356-6_1
57. Shoji, T. & Tsuboi, Y. Plasmonic optical tweezers toward molecular manipulation: Tailoring plasmonic nanostructure, light source, and resonant trapping. *J. Phys. Chem. Lett.* **5**, 2957–2967 (2014).
58. Juan, M. L., Gordon, R., Pang, Y., Eftekhari, F. & Quidant, R. Self-induced back-action optical trapping of dielectric nanoparticles. *Nat. Phys.* **5**, 915–919 (2009).
59. Pang, Y. & Gordon, R. Optical trapping of 12 nm dielectric spheres using double-nanoholes in a gold film. *Nano Lett.* **11**, 3763–3767 (2011).
60. Haitian, X., Jones, S., Choi, B.-C. & Gordon, R. Characterization of Individual Magnetic Nanoparticles in Solution by Double Nanohole

- Optical Tweezers. *Nano Lett.* **16**, 2639–2643 (2016).
61. Jones, S., Al Balushi, A. A. & Gordon, R. Raman spectroscopy of single nanoparticles in a double-nanohole optical tweezer system. *J. Opt.* **17**, 1–5 (2015).
 62. Jones, S., Andr en, D., Karpinski, P. & K all, M. Photothermal Heating of Plasmonic Nanoantennas: Influence on Trapped Particle Dynamics and Colloid Distribution. *ACS Photonics* **5**, 2878–2887 (2018).
 63. Akemann, W. & Otto, A. Continuous secondary light emission from silver films: on the origin of the inelastic background in SERS. *Surf. Sci.* **307–309**, (1994).
 64. Apell, P., Monreal, R. & Lundqvist, S. Photoluminescence of noble metals. *Phys. Scr.* **38**, 174–179 (1988).
 65. Lin, K. *et al.* Plasmonic photoluminescence for recovering native chemical information from surface-enhanced Raman scattering. *Nat. Commun.* **8**, 1–9 (2017).
 66. Ma, Z. *et al.* Origin of the Avalanche-Like Photoluminescence from Metallic Nanowires. *Sci. Rep.* **6**, 1–10 (2016).
 67. Haug, T., Klemm, P., Bange, S. & Lupton, J. M. Hot-Electron Intraband Luminescence from Single Hot Spots in Noble-Metal Nanoparticle Films. *Phys. Rev. Lett.* **115**, 1–5 (2015).
 68. Ikeda, K., Suzuki, S. & Uosaki, K. Enhancement of SERS background through charge transfer resonances on single crystal gold surfaces of various orientations. *J. Am. Chem. Soc.* **135**, 17387–17392 (2013).
 69. Hugall, J. T. & Baumberg, J. J. Demonstrating Photoluminescence from Au is Electronic Inelastic Light Scattering of a Plasmonic Metal: The Origin of SERS Backgrounds. *Nano Lett.* **15**, 2600–2604 (2015).
 70. Otto, A., Timper, J., Billmann, J., Kovacs, G. & Pockrand, I. Surface roughness induced electronic raman scattering. *Surf. Sci.* **92**, 55–57 (1980).
 71. Portales, H. *et al.* Raman scattering by electron-hole excitations in silver nanocrystals. *Phys. Rev. B* **63**, 233402 (2001).
 72. Barnett, S. M., Harris, N. & Baumberg, J. J. Molecules in the mirror: How SERS backgrounds arise from the quantum method of images. *Phys. Chem. Chem. Phys.* **16**, 6544–6549 (2014).
 73. Huang, T. & Murray, R. W. Visible luminescence of water-soluble monolayer-protected gold clusters. *J. Phys. Chem. B* **105**, 12498–12502 (2001).
 74. Beversluis, M. R., Bouhelier, A. & Novotny, L. Continuum generation

References

- from single gold nanostructures through near-field mediated intraband transitions. *Phys. Rev. B* **68**, 115433 (2003).
75. Cai, Y. Y. *et al.* Anti-stokes emission from hot carriers in gold nanorods. *Nano Lett.* **19**, 1067–1073 (2019).
 76. Xie, X. & Cahill, D. G. Thermometry of plasmonic nanostructures by anti-Stokes electronic Raman scattering. *Appl. Phys. Lett.* **109**, 1–5 (2016).
 77. Carattino, A., Caldarola, M. & Orrit, M. Gold nanoparticles as absolute nano-thermometers. *Nano Lett.* **18**, 874–880 (2017).
 78. Goodwin, P. M., Ambrose, W. P., Martin, J. C. & Keller, R. a. Spatial dependence of the optical collection efficiency in flow cytometry. *Cytometry* **21**, 133–44 (1995).
 79. Enderlein, J. & Ambrose, W. P. Optical collection efficiency function in single-molecule detection experiments. *Appl. Opt.* **36**, 5298–302 (1997).
 80. Iacopini, S. & Piazza, R. Thermophoresis in protein solutions. *Europhys. Lett.* **63**, 247–253 (2003).